Wave–structure interaction by a two–way coupling between a fully nonlinear potential flow model and a Navier–Stokes solver

Paul Landesman, Jeffrey Harris, Christophe Peyrard, Michel Benoit

Ocean Engineering 308 (2024) 118209

Contents lists available at ScienceDirect

Ocean Engineering

journal homepage: www.elsevier.com/locate/oceaneng

Research paper

Wave–structure interaction by a two–way coupling between a fully nonlinear potential flow model and a Navier–Stokes solver

Paul Landesman [a,b], Jeffrey C. Harris [b,*], Christophe Peyrard [a,b], Michel Benoit [a,b]

[a] LHSV, Ecole des Ponts, EDF R&D, Chatou, France
[b] Laboratoire National d'Hydraulique et Environnement (LNHE), EDF R&D, Chatou, France

ARTICLE INFO

Keywords:
Fully nonlinear potential flow
Wave–structure interaction
Computational fluid dynamics

ABSTRACT

A two-way domain decomposition coupling procedure between a fully nonlinear potential flow model and a Navier–Stokes solver capturing the free surface with a Volume of Fluid method is used to study wave–structure interaction applied to offshore wind turbines. Away from the structure, the large-scale inviscid wave field is modeled by the potential code. Wave generation and absorption in this 3D hybrid model take place in the outer potential domain. The codes exchange data in the region around their common boundaries. Through the two-way coupling, waves propagate in and out of the viscous subdomain, making the hybrid algorithm suitable to study wave diffraction on marine structures, while keeping the viscous subdomain small. Each code uses its own mesh and time step. Subdomains are overlapping, therefore continuity conditions on velocity and free surface have to be verified on two distinct coupling surfaces at any time. Parallel implementation with communications between the models relying on the Message Passing Interface library allows calculations on large spatial and temporal scales. The coupling algorithm is first tested for regular nonlinear waves and then applied to simulate wave loads exerted on a vertical monopile in 3D. Attention is paid to the high-order components of the horizontal force.

1. Introduction

Among the decarbonized power sources needed to meet the requirements of the United Nations's Paris Agreement (United Nations, 2015) on mitigating global warming, Offshore Wind Turbines (OWT) are an attractive option and a fast-developing industrial sector. With an installed capacity of 25 GW as of 2020, OWT already represent 12.9% of the total wind power capacity (194 GW) (Wind Europe, 2021).

Depending on the local water depth, either fixed or floating OWT solutions can be deployed. Whatever the retained solution, OWT structures should withstand various mechanical loads, originating from wind, waves or ocean currents, in particular in extreme (storm) conditions. Among these, the wave loads are usually the most prominent ones. For that purpose, analytical, experimental and numerical investigations are conducted in the design phase of OWT foundations or floaters. Due to the diversity and complexity of the physical phenomena related to wave–structure interaction, analytical, or semi-analytical approaches, such as the Morison equation (Morison et al., 1950), albeit widely used in the industry, are limited to small wave steepness.

Model-scale experiments, on the other hand, account for the full physics and remain a valuable option for the validation of numerical models used in the design process, in particular for floating foundations or in case of specific nonlinear wave loads, like breaking loads. They are however time-consuming and costly, and do not always allow for an accurate assessment of certain wave-induced flow properties, such as complex three-dimensional (3D) velocity fields or hydrodynamic pressure levels on a structure. Furthermore, scale effects might deteriorate the quality of results, in particular regarding damping.

Numerical methods of OWT design provide access to any variable of interest in the whole computational domain at prototype scale, and are less expensive than experimental campaigns. However, as the most widely used engineering tools rely on the Morison equation for the hydrodynamic part, which only takes incident wave kinematics into account, not all physical phenomena can be simulated and various approximations are made. This way, low computational costs are obtained. Indeed, the drag force exerted on the structure is estimated from a drag coefficient (possibly as a function of flow conditions),

* Corresponding author.
E-mail addresses: jeffrey.harris@enpc.fr (J.C. Harris), christophe.peyrard@edf.fr (C. Peyrard), michel.benoit@edf.fr (M. Benoit).

https://doi.org/10.1016/j.oceaneng.2024.118209
Received 24 December 2023; Received in revised form 15 April 2024; Accepted 16 May 2024

the wave diffraction is modeled by a single coefficient, and the wetted area is approximated. One should ensure that such numerical results are relevant and capture the main physical processes, like drag and inertia forces for hydrodynamics, thrust and wake description for aerodynamics. Although many case-specific modifications exist, essentially the Morison equations are based on integrating two-dimensional strips of the geometry, generally ignoring three-dimensional effects. Recently approaches for including slamming loads in this type of semi-empirical formulations have been developed, but require calibration as well (Renaud et al., 2023).

This makes necessary the development and use of higher fidelity models, e.g. based on Computational Fluid Dynamics (CFD) approaches, in order to identify the domain of validity of design models. As very different time and space scales are involved, this might call for the use of very fine time and space discretizations, and lead to unrealistic computational costs. Numerical methods allowing for a reduced computational burden are then sought that also keep sufficient accuracy.

Hence, coupling a potential wave model accurately describing large-scale wave propagation and a viscous CFD solver simulating the main physical phenomena related to wave–structure interaction at the local scale is an interesting option. This is the major motivation of this work aiming at developing and validating a two-way coupling strategy between a Fully Nonlinear Potential Flow (FNPF) solver and a Navier–Stokes (NS) solver. A 3D two-way coupled model is developed, with the goal of applying it to wave-interaction problems of large spatial and temporal scales involving fixed structures. To that end, attention is paid to the flexibility of the designed hybrid strategy and its suitability for the simulation of various wave-induced flows. The accuracy and stability properties of the simulated cases are investigated in detail, as well as several related numerical challenges. Parallelization of the hybrid procedure is ensured so that the method can be applied to 3D cases of potential interest for the engineer. Complex model layouts are also considered, involving more than one instance of each code.

The remainder of this article is organized as follows: in Section 2 a literature review is presented covering potential, viscous and hybrid (i.e. coupled) approaches. The FNPF and NS models selected in the present study are briefly described in Section 3, while the proposed two-way coupling strategy is presented in Section 4. The hybrid model is then applied and validated with 2DV (two-dimensional vertical) regular wave cases in Section 5. Coupled 3D simulations of diffraction of regular nonlinear waves on a vertical cylinder are performed in Section 6, and compared with wave tank experiments. Conclusion and outlook for future work are given in Section 8.

2. Literature review of coupling methods

Among hybrid techniques previously applied to water waves propagation and wave–structure interaction simulation, that rely on the near-field/far-field distinction, different global approaches can be distinguished. In this paper, we will restrict our attention to couplings between potential flow and Navier–Stokes models.

Wave propagation and wave transformation on a varying bottom over large distances in finite depth, among other problems, are efficiently handled by mathematical models devoted to the description of incompressible and irrotational (hence kinematically inviscid) flows, namely potential free surface models, such as reviewed by Dias and Bridges (2006). In these models, a Laplace equation on the velocity potential for mass conservation is solved in a domain in which free surface position is not known *a priori*. Indeed, nonlinear kinematic and dynamic boundary conditions govern the time-evolution of the free surface shape and potential at the free surface. Other linear conditions complete the set of boundary equations to yield a Boundary Value Problem (BVP) to be resolved at every considered time instant, leading to so-called FNPF models. For this paper, a Boundary Element Method (BEM) formalism will be used. Green's second identity is used to express the velocity potential anywhere inside the water volume as a function of the potential and its normal derivative on the fluid domain boundaries, in the form of Boundary Integral Equations (BIE). Physical assumptions made to characterize the flow on every domain boundary translate into Dirichlet and Neumann conditions on the velocity potential, and possibly on its time derivative. The above-mentioned fully-nonlinear kinematic and dynamic free surface boundary conditions yield, through a time-stepping procedure, a Dirichlet condition for the potential (and its time derivative), whereas Neumann conditions are imposed on all other boundaries.

Even with fully-nonlinear models, the potential flow assumption inherently prevents from describing rotational, viscous, and turbulent effects experienced near the structures of interest. A precise description of wave-induced flows in the neighborhood of a fixed or moving structure requires the solution of the full Navier–Stokes (NS) equations to account for rotational, viscous, and possible turbulent effects. Though many models exist, in this paper, we focus on just the Volume Of Fluid (VOF) method, following the pioneering work of Hirt and Nichols (1981), in the CFD code code_saturne (CS). The use of these high-fidelity CFD models to simulate free surface flows over large temporal and spatial scales is limited, as already stated, by the large associated computational costs. These methods also suffer from possibly excessive numerical diffusion levels, hence they are not as accurate as the potential models to simulate wave propagation over large distances. This explains why hybrid or coupled methods, either based on Functional Decomposition (FD) or Domain Decomposition (DD), have been used to solve large scale wave-induced flows.

Physical assumptions made in both near-field and far-field models may differ: although in the majority of far-field models a potential flow is considered, in certain cases Euler equations are solved instead, allowing to represent rotational effects (Di Paolo et al., 2021). The scope is here limited to studies involving the resolution of NS equations in the near-field domain, although investigations have been reported that use potential methods of uneven accuracy levels and CPU costs to describe flows in both regions (Ferrant, 1998; Bai and Eatock Taylor, 2007). When it comes to solving the near-field wave problem then, the diversity of NS numerical methods is reproduced in hybrid approaches.

Discrepancies are also related to the extent of numerical domains where the respective sets of equations are solved. Indeed, the use of a DD method, as its name suggests, involves that in most of the global simulation domain the description of the flow is provided by only one model. Solvers thus exchange information at their coupled boundaries. On the other hand, in FD approaches, where variables of interest (namely velocity, pressure, free surface position or phase function) are decomposed into a part related to the incident (as well as, possibly, diffracted) wave field, and a complementary one taking into account the remaining wave–structure interaction phenomena, potential and NS equations are solved over fully overlapped domains. Nested domain-decomposition techniques are singular in that the small CFD domain of a limited extent is enclosed in a wider far-field domain, thus it implies that the corresponding part of the far-field domain is not taken into account in the simulation. If near-field to far-field feedback is made possible, near-field variables should be imposed to the outer solver in the interior of its numerical domain.

A last criterion that significantly differentiates coupling strategies is whether simulation data are only transmitted from the far-field to the near-field model (one-way coupling), or whether the opposite is also true (two-way coupling). A one-way coupling methodology enables a preliminary computation of the outer wave field, as near-field feedback is not provided during the simulation. In two-way coupling techniques, reflected, diffracted or radiated waves might be dealt with in the far-field model. Therefore it allows for a reduction of the near-field domain's size, as compared to one-way hybrid methods where waves scattered by a structure can only be simulated in the inner region. This also comes at the cost of extra implementation choices and challenges, and possible stability issues. In the following, a literature review is conducted on the basis of this classification.

FD based couplings. FD methods have been successfully applied to a number of wave-body interaction cases. The Spectral Wave Ex-

plicit Navier–Stokes Equations (SWENSE) method is one of the most prominent FD, also called perturbation, approach. Among numerous other works, it enabled the simulation of a bottom-mounted circular cylinder in regular nonlinear waves (Gentaz et al., 2004) as well as that of a captive buoy with a heaving skirt subject to plane regular and irregular multidirectional waves (Monroy et al., 2011). It consists of a combination of a fully nonlinear potential spectral model with a one-phase or two-phase Reynolds Averaged Navier–Stokes Equations (RANSE) solver (several models have been used). It should be noted that the far-field model only accounts for the incident wave field, due to the spectral formalism, in which only symmetrical or periodic domains can be represented. Hence, the far-field potential calculation can be run prior to the viscous near-field one.

General considerations about FD methods, as well as an implementation with OceanWave3D as the comprehensive model to treat wave-body interactions, are reported in Ducrozet et al. (2014). It should be mentioned that this technique permits all physical phenomena related to wave-body interactions, as well as nonlinear wave-wave and wave-bottom interactions. Therefore, it belongs to the class of "strong" couplings that can simulate large scattered wave fields away from the body. Nonlinear interactions between waves and uneven bottom, if not accounted for by the far-field solver, as well as nonlinear interactions between incident and scattered waves, are indeed described by the viscous CFD model without any restrictive hypothesis. In the SWENSE formalism, this means that the refined part of the RANSE mesh, in which the latter effects operate, should have its size adapted to its expected spatial extent. It is therefore very well adapted, in the context of wave–structure interaction, to the description of problems involving small bodies, in which the incident flow is not disturbed much and viscous effects are predominant, while the occurrence of diffraction and radiation phenomena are limited to the body's vicinity. Small body problems are characterized by large Keulegan–Carpenter numbers ($KC = \frac{2\pi A}{D}$, where A is the incident wave amplitude and D the characteristic size of the structure). The larger the structure, the smaller the KC, and the larger the diffraction/radiation effects. To deal with this latter case in the SWENSE framework or with related methods, it is necessary to increase the size of the refined part of the RANSE grid to allow for physically accurate computations. This leads to growing mesh sizes and CPU time requirements, minimizing the gains brought about by the coupling. If the refined part of the RANSE grid is too small, waves are damped in an unphysical manner while traveling on coarser parts of the mesh. It would be interesting to compare the relative performances of FD methods and two-way DD ones in such cases, as in the latter nonlinear wave-wave interactions are dealt with in the computationally less demanding far-field model.

A perturbation approach is used in Harris and Grilli (2012) to simulate wave-induced boundary layer flows, where a 2D FNPF-BEM solver is coupled to a 3D NS model. Recently, Robaux (2020) and Robaux and Benoit (2022) proposed a FD model coupling a 2DV HPC potential model with a RANSE VOF solver of OpenFOAM. Similarly, this kind of approach was studied by O'Reilly et al. (2022). The HPC formalism represents interactions of waves with possibly moving and surface-piercing structures in the potential flow model. In the mentioned works, only cases involving fixed 2D fully-submerged bodies were investigated. Therefore, it considers an incident wave field, as well as the fully-nonlinear potential diffracted wave field. Thus, larger values of KC might be considered without an excessive penalty on computational cost, as long as viscous and turbulent effects on the scattered wave field are restricted to the vicinity of the body.

One-way coupling DD approaches. One-way DD coupling techniques, as they only require the transfer of information from the far-field to the near-field model, are easier to implement than two-way DD methods. For this reason, a large number of authors have applied them to wave-induced flows occurring in ocean or coastal engineering. Therefore, we do not intend to be exhaustive here, and only a few works related to wave-body interactions are presented.

Guignard et al. (1999) computed the shoaling of solitary waves on a mild slope through a BEM/VOF hybrid one-way 2D approach. Hildebrandt and Sriram (2014) studied pressure distribution on and vortex shedding behind a bottom-mounted vertical circular cylinder impacted by steep focused waves combining a FEM potential model and a commercial RANSE solver. Numerical results were compared to experimental ones. Similarly, Paulsen et al. (2014) used OceanWave3D and a VOF solver from OpenFOAM to study wave loads on a surface-piercing cylinder standing for an offshore wind turbine foundation, under different wave conditions and bottom configurations. Using the same tool, Veic and Sulisz (2018) investigated pressure distribution from irregular breaking waves on a monopile with the same setup. A 3-hour storm was simulated in the potential model and the impact of the highest breaking wave was then numerically reproduced.

For more recent works, note also that Robaux (2020) and Robaux and Benoit (2022) implemented both FD and one-way DD methods, and compared them on the case of waves diffracted by a submerged fixed body. Batlle Martin et al. (2022) and Batlle Martin et al. (2023) considered a one-way DD with *CS* for breaking focused waves.

Two-way coupled methods. As not so many two-way coupled models have been reported so far, in this section the scope of considered applications is widened beyond wave-body interactions in finite water depth. Some of the earliest two-way hybrid approaches were reported for steady free surface problems. Campana et al. (1995) and Chen and Lee (1999) studied the flow past a ship advancing at a constant speed using overlapping domain decomposition methods, with linear and nonlinear assumptions for the free surface boundary conditions, respectively.

Iafrati and Campana (2003) computed wave-breaking 2D flows with a two-way coupled method, in which free surface is enclosed in the viscous top domain, while a Laplace equation on the potential is solved in a region underneath the latter. In this paper, a further distinction is established among two-way coupling methods, that we endorse and employ to describe and sort other two-way hybrid studies. For the sake of simplicity, we restrict the description to the case of a single coupling region. Iafrati and Campana (2003) state that, depending on whether near-field and far-field numerical domains are overlapped or not, different sets of coupling transmission conditions should be specified on their common boundary(ies). In both situations, continuity of the velocity should be ensured on the near-field or common matching surface, therefore all components of the potential far-field velocity vector are sent to the near-field NS model to be used as Dirichlet boundary condition on the viscous velocity. If both domains overlap, a kinematic condition imposing the continuity of the normal velocity on the far-field boundary should be set. This amounts to a heterogeneous Neumann boundary condition on the velocity potential, thus the overlapping domain decomposition coupling is called "Neumann type" (NT) coupling. If, alternatively, a common coupling boundary is used, the velocity continuity condition already mentioned is complemented by a normal stress continuity condition, through which pressure from the RANSE solver is imposed to the outer potential model. By integrating Bernoulli's equation, a Dirichlet condition on the velocity potential is obtained on the unique coupling boundary ("Dirichlet type" coupling (DT)). Note that nothing is said about the free surface, as it is totally enclosed in the viscous domain. Whatever the coupling type, an iterative time-stepping procedure is followed in Iafrati and Campana (2003) to enforce the continuity requirements.

Lachaume et al. (2003) briefly discuss two-way coupled simulations of a solitary wave shoaling over a plane slope, in which the free surface is described in both models. The BEM model of Grilli et al. (2001) is combined with a VOF instance, but very few results are displayed, and for the considered case a one-way coupling approach seems to be sufficient. Greco et al. (2002) applied a DT coupling between BEM and VOF models to dam-breaking and water loading on deck structure 2D problems involving complex free surface geometries. Again, and

as for all the remaining studies addressed in this section, the free surface is split between near-field and far-field wave models. Alongside experimental results, a comparison of DT and NT coupling VOF-based techniques is realized in Greco (2002) in the same context. The NT coupling, albeit less computationally efficient than the DT coupling, is found to successfully simulate a wave-induced flow oriented towards the outer region, whereas the DT coupling fails. A NT strategy is thus retained and described in detail in Colicchio et al. (2006), involving two-phase BEM and NS-LS models. Further explanations are given as to the advantages of the NT technique over the DT one, in terms of allowed flexibility of spatial discretizations in each model. It should be noted that the NT coupling procedure differs from the one presented in Iafrati and Campana (2003) as information on free surface position and orientation, but also pressure values are exchanged between coupled models. This way a Neumann boundary condition on the time derivative of the potential in the BEM model is available. An intrinsic algorithm is used for time integration, in which time stepping schemes of BEM and NS-LS models are linked. At several instants per time step, both sub-domains successively exchange coupling variables. This is made possible by the fact that they share the same time-step size. Siddiqui et al. (2018), from the same research group, used a HPC-VOF DT coupling method to simulate the 2D behavior of a damaged ship section in forced heave motion. Coupled models still share the same time step size, but time marching is done separately and coupling information is exchanged only once per time step through the matching boundary. Following the work of Colicchio et al. (2006), a NT coupling involving HPC and single phase NS-LS models is presented in Hanssen (2019) and applied to the 2D propagation of regular waves.

A 2D BEM-VOF NT hybrid model is presented in Kim et al. (2010), and successfully applied to nonlinear regular and irregular wave propagation problems. It features several noteworthy characteristics. Indeed, both models use different spatial and temporal resolutions, such that the BEM time step equals an integer multiple N of the NS-VOF one. Hence, the exchange of coupling data at both ends of the overlapping region occurs once every N VOF time steps, and the coupling procedure is not iterative. Moreover, the BEM free surface in the latter part of the domain is relaxed towards the VOF solution to ensure continuity. Changes made to the velocity potential at the free surface account for this modification of the free surface shape. Hybrid simulation results are compared to those of VOF-only computations and equivalent accuracy levels are observed, for a fraction of the computational time.

Another 2D BEM-VOF model similar to that of Kim et al. (2010) is proposed by Guo et al. (2012). As in Kim et al. (2010), a low-order in space fully nonlinear potential model is coupled with a NS-VOF solver. The verification of the coupled model is done with regular wave propagation and full reflection cases, prior to its application to the simulation of regular nonlinear wave impacts on a fixed horizontal plate. A non-overlapping DT coupling is implemented by Zhang et al. (2013) and tested on 2D dam-break and solitary wave propagation over constant depth cases. Lu et al. (2017) is one of the few reported 3D two-way couplings. It is of Neumann type, combines potential and viscous solvers both based on Finite Volume formalism and relies heavily on the OpenFOAM toolbox. 2D cases of solitary wave propagation, regular wave forces on a fixed partly-submerged barge, and regular shallow-water waves shoaling and breaking on a slope are investigated, whose results are compared to theoretical and experimental references. At last, a qualitative study of the motion and subsequent radiated wave field of a freely falling 3D object is presented. This last article might well be the one with which the present study is the most closely related.

Two-way hybrid models involving shallow-water models and more comprehensive RANS models have been developed and successfully applied to 2D shallow-water wave flows by Sitanggang and Lynett (2010) and Pringle et al. (2016). Mintgen and Manhart (2018) used a Shallow-Water Equations (SWE) 2D solver combined with a VOF module for surface capturing in 3D in OpenFOAM to simulate wave propagation and wave–structure interactions. It should be noted that in this work, the direction of the transfer of coupling information depends on the instantaneous nature of the flow.

Several authors have investigated hybrid methods combining a potential model and a meshless Lagrangian NS solver. Sueyoshi et al. (2007) simulated 2D wave-body interactions with a BEM model and a Moving Particle Semi-Implicit (MPS) method, with a top-bottom domain decomposition approach inspired by that of Iafrati and Campana (2003). A novel moving overlapping zone is implemented in Sriram et al. (2014) to build a NT hybrid method between a FEM potential model and an Improved Meshless Local Petrov Galerkin method with Rankine source solution (IMLPG_R) to simulate the propagation and breaking of 2D waves. Similarly, Yan and Ma (2017) simulate 2D non-breaking focused waves. Verbrugghe et al. (2018) built a two-way coupling strategy in which the numerical domain of OceanWave3D, the large scale fully-nonlinear potential model, encloses a small SPH (DualSPHysics) domain. Horizontal velocity is transmitted to SPH boundaries. The two-way coupling is however not complete, as only the free surface position is transmitted to the potential model from the SPH instance. The method is verified with regular wave propagation cases, then applied in 2D to the simulation of a fixed oscillating water column and a floating box in waves. 3D simulations of a heaving cylinder in waves presented in Verbrugghe et al. (2019) are realized with a one-way coupling approach only.

Hamilton and Yeung (2011) simulated the diffraction of linear plane waves by a vertical cylinder with a singular two-way coupling method that could be considered of Dirichlet type. Shell functions in a polar coordinate system are used to characterize a linear outer wave-induced potential flow coupled with an inner one-phase viscous solution, through a vertical cylinder matching boundary. It should be noted that the NS solver also makes use of linearized free surface boundary conditions. Kemper et al. (2019) developed a DD method in which a small OpenFOAM NS-VOF domain is nested in a larger FDM OceanWave3D domain. It was applied to 2D wave propagation over a submerged bar. Recently, a somewhat different 2D-3D coupling strategy involving OpenFOAM instances was reported by Di Paolo et al. (2021). Plane-wave generation and propagation are done in a NS-VOF 2DV domain while interaction with structures is dealt with using the same solver but accounting for 3D effects.

From this review, it appears that although 3D one-way DD and FD hybrid methods have been successfully applied to a number of different wave-body interaction problems, the same cannot be said of two-way DD techniques. The vast majority of investigations indeed involve 2DV domains, and only recently have 3D cases been reported. For example, the sinking semi-submersible platform in the study of Lu et al. (2017) was not compared to reference results. Now, however, more advanced 3D two-way couplings, like that of Saincher and Sriram (2022), show the possibilities compared to laboratory experiments. Nevertheless, there seems to be room for improvements and validated applications to 3D cases.

3. Potential flow and NS solver description

3.1. Description of the FNPF solver *seine3d*

The far-field flow solver in the two-way hybrid strategy implemented in the current work is referred to as *seine3d*, and uses a higher-order BEM approach. For a more in-depth presentation of this model, the reader is referred to Grilli et al. (2001) and Harris et al. (2022).

3.1.1. Governing equations

As stated above, we consider the irrotational flow of an incompressible and inviscid fluid as a physical model for wave-induced water flows. Mass conservation in the fluid domain Ω yields the following Laplace equation:

$$\nabla^2\phi = 0 \qquad \text{in } \Omega \tag{1}$$

$$\mathbf{u} = \nabla\phi \qquad \text{in } \Omega \tag{2}$$

with ϕ the velocity potential and $\mathbf{u}$ the flow velocity in Ω. From Green's second identity, it comes that Eq. (1) is changed into a BIE to be verified on the domain boundary Γ, at a collection of collocation points $\mathbf{x}_i$ $(i = 1, \dots, N_\Gamma)$,

$$\alpha(\mathbf{x}_i)\phi(\mathbf{x}_i) = \int_\Gamma \left[\frac{\partial\phi}{\partial n}(\mathbf{x})G - \phi(\mathbf{x})\frac{\partial G}{\partial n}\right] \mathrm{d}\Gamma, \tag{3}$$

where α is the interior solid angle made by the boundary at $\mathbf{x}_i$ (equal to 2π if the surface is smooth), $\mathbf{n}$ the outwards normal vector to the boundary at point $\mathbf{x}$ and G the 3D free space Green's function of Laplace's equation, based on the distance $r_i = \|\mathbf{x} - \mathbf{x}_i\|$ from point $\mathbf{x}_i$ to point $\mathbf{x}$ on the boundary. The Green's function satisfies the following relations:

$$G(\mathbf{x} - \mathbf{x}_i) = \frac{1}{4\pi\, r_i} \tag{4}$$

$$\frac{\partial G}{\partial n}(\mathbf{x} - \mathbf{x}_i) = -\frac{(\mathbf{x} - \mathbf{x}_i)\cdot\mathbf{n}}{4\pi\, r_i^3} \tag{5}$$

Under the same set of assumptions, the integrated form of the momentum conservation equation reduces to the generalized unsteady Bernoulli equation, which reads, at all times:

$$\frac{\partial\phi}{\partial t} = -gz - \frac{1}{2}\nabla\phi\cdot\nabla\phi - \frac{p}{\rho} \qquad \text{in } \Omega \tag{6}$$

with g the gravitational acceleration, z the vertical coordinate, p the fluid pressure assumed to be constant on the free surface, and ρ the fluid density. Eq. (6), yields the dynamic free surface boundary condition prescribed on the air–water interface, used in combination with a kinematic free surface boundary condition expressing that free surface Γ_f is advected with the flow.

The nonlinear Eq. (6), once integrated in time, yields a Dirichlet condition on ϕ on the free surface whose geometry is computed by tracking free surface nodes in time. Other typical boundary conditions include homogeneous Neumann conditions on ϕ on the vertical lateral faces and bottom region enclosing Ω, expressing the impermeability of these walls. In certain cases, these are complemented by a heterogeneous Neumann condition on a part of the domain dedicated to wave generation, either vertically fixed or moving. Wave kinematics from various wave theories might indeed be enforced on a vertical boundary, or alternately a realistic wavemaker motion might be reproduced (see Grilli and Horrillo, 1997 for details about wave generation). As only far-field waves are investigated in *seine3d* in the current work, there is no need to represent submerged or surface-piercing, fixed or floating bodies in Ω, thus we have a complete set of boundary conditions available, ensuring the well-posedness of the problem. Given that suitable initial conditions are provided, as well as a spatial discretization of the boundaries and a time-stepping strategy, simulation of potential wave flow through time is made possible.

3.1.2. Time integration scheme

The resolution of the BIE at any time instant t yields both ϕ and its normal derivative ϕ_n at every node $\mathbf{x_i}$ of the free surface. Time integration of free surface boundary conditions is then needed to advance the solution (geometry alongside with boundary conditions) in time. This is done following a Mixed Eulerian-Lagrangian (MEL) method, originally introduced by Longuet-Higgins and Cokelet (1976). Here another hypothesis is made as to the nature of the flow and the geometry of the free surface. The latter is indeed assumed to be single-valued. Since the most complex interface shapes are expected in the near-field domain treated with *CS*, this should have a negligible influence on the range of applications of the hybrid method. Thus we opt for a semi-Lagrangian time updating scheme for Γ, for which free surface nodes are only allowed to move vertically, which makes mesh handling easier. The material derivative can then be written:

$$\frac{\delta}{\delta t} = \delta_t = \frac{\partial}{\partial t} + \frac{\partial\eta}{\partial t}\frac{\partial}{\partial z} \tag{7}$$

where $\eta = \mathbf{r}\cdot\mathbf{k}$ denotes the vertical free surface elevation, $\mathbf{k}$ being the vertical unit vector.

Making use of this formalism in Eq. (6) leads to:

$$\frac{\delta\eta}{\delta t} = \frac{\partial\phi}{\partial z} - \frac{\partial\phi}{\partial x}\frac{\partial\eta}{\partial x} - \frac{\partial\phi}{\partial y}\frac{\partial\eta}{\partial y} \qquad \text{at } z = \eta \tag{8}$$

$$\frac{\delta\phi}{\delta t} = -g\eta - \frac{1}{2}\nabla\phi\cdot\nabla\phi + \frac{\partial\eta}{\partial t}\frac{\partial\phi}{\partial z} - \frac{p}{\rho} \qquad \text{at } z = \eta \tag{9}$$

where the atmospheric pressure, p, is taken without loss of generality to be zero. It should be noted that $(\partial\eta/\partial x, \partial\eta/\partial y)$ might be rewritten using components of the outward normal vector on Γ_f, $\mathbf{n} = (n_x, n_y, n_z)$, yielding $(-n_x/n_z, -n_y/n_z)$.

A third-order explicit Runge–Kutta scheme, inspired from that of Gottlieb (2005), is chosen to integrate Eqs. (8) and (9) in time. Alongside with ϕ and ϕ_n, their respective time derivatives might also be needed if one wants to use another time-stepping scheme, such as an explicit Taylor series expansion (again, see Grilli et al., 2001 for example). Besides this, the computation of forces and moments exerted on structures is realized through pressure integration on the body's surface (obtained from Eq. (6)), therefore wave–structure interaction studies also require the resolution of a second Laplace equation for ϕ_t. As only the third-order Runge–Kutta scheme is considered in the present work, and no structure is considered in the potential region, this is not needed.

Additionally, it should be noted that a careful computation of the tangential derivatives of ϕ is needed on Γ_f to express certain terms of (8) and (9). For brevity, the discretized equations are not presented here. Spatial discretization of the numerical domain boundaries relies on B-spline elements, described in depth in Harris et al. (2022).

3.2. Description of the NS solver code_saturne

The near-field flow solver in the current work is the NS solver *code_saturne* (*CS*). *CS* is an open-source, multi-purpose CFD code aimed at solving the full NS equations, for either incompressible or weakly compressible flows, through a Finite Volume approach with co-located variables. Equations are integrated in time according to a predictor/corrector method. The code deals with structured as well as unstructured meshes and was recently enriched with an algebraic VOF module for interface-capturing purposes in multiphase simulations. Numerous turbulence models are available to be used with RANS or LES (large eddy simulation) formalisms, although in this work no turbulence model is used. Also, as will be detailed later, structured grids are used exclusively. The VOF module was added to *CS* alongside with the release of version *5.0.0* in 2017. All *CS*-based developments reported in this article rely on the stable version *6.0.0*.

3.2.1. Governing equations

If gravity is the only external force, the NS equations for continuity and momentum respectively are:

$$\frac{\partial\rho}{\partial t} + \nabla\cdot(\rho\mathbf{u}) = 0 \tag{10}$$

$$\frac{\partial\rho\mathbf{u}}{\partial t} + \nabla\cdot(\rho\mathbf{u}\otimes\mathbf{u}) = -\nabla p + \nabla\cdot\mathbb{T} + \rho\mathbf{g} \tag{11}$$

with ρ the fluid density, $\mathbf{u}$ the velocity, $\rho\mathbf{u}$ the volume momentum quantity, and $\mathbb{T}$ the deviatoric stress tensor while $\otimes$ is the tensor product. Note that surface tension is neglected. For simplicity, possible additional source terms are not taken into account. Assuming a Newtonian fluid, $\mathbb{T} = \mu\left[\nabla\mathbf{u} + \nabla\mathbf{u}^T\right] - \frac{2}{3}\mu(\nabla\cdot\mathbf{u})\mathbb{I}$, where $\mu = \rho\nu$ is the dynamic viscosity.

The VOF method enables the simulation of multiphase flows with a one-fluid formalism, by describing the phase content of any fluid region from volume fractions of the different phases. In the context of wave-induced free surface flows, only two immiscible phases are considered, namely air and water. Hence, α is defined as the volume fraction of air or void fraction:

$$\alpha = \frac{\text{void/air volume in a cell}}{\text{volume of the cell}} \tag{12}$$

Using Eq. (12), linear mixture properties laws are established so that ρ and μ are continuously defined throughout the fluid. Subscripts $_{water}$ and $_{air}$ designate respective phases.

$$\rho = \alpha\rho_{air} + (1-\alpha)\,\rho_{water} \tag{13}$$

$$\mu = \alpha\mu_{air} + (1-\alpha)\,\mu_{water} \tag{14}$$

For all cases considered here, the density values are set to $\rho_{water} = 1025$ kg/m^3 and $\rho_{air} = 1$ kg/m^3, while the dynamic viscosity values are $\mu_{water} = 1\times10^{-3}$ Pa s and $\mu_{air} = 1\times10^{-5}$ Pa s. Assuming that both ρ_{water} and ρ_{air} are constant, Eq. (10) for mass conservation can be simplified to

$$\nabla\cdot\mathbf{u} = 0 \tag{15}$$

$$\frac{\partial\alpha}{\partial t} + \nabla\cdot(\alpha\mathbf{u}) = 0 \tag{16}$$

For an easier definition of boundary conditions, the relative pressure $p^* = p - \rho_{air}\mathbf{g}\cdot\mathbf{x} - p_0$ is introduced, where p_0 is the reference pressure at a fixed arbitrary location. However, for the sake of clarity, p^* is denoted p hereafter.

3.2.2. Time stepping scheme

The time-stepping method to advance the VOF solution in time is based on the fractional step scheme of Chorin (1968) and can be associated with the SIMPLEC scheme (Versteeg and Malalasekera, 2007). More details on this topic can be found in Archambeau et al. (2004). This last reference, alongside with *CS*'s theory guide (Code Saturne development team, 2019), should also be used for an in-depth description of spatial discretization strategies, and the discretized equations are not recalled here for brevity.

Prediction step. A prediction step is conducted to integrate the momentum balance Eq. (11) with an explicit pressure gradient. Mass fluxes are also treated explicitly, while an implicit form of the viscous diffusive term is used. This first step allows computing a predicted velocity field $\mathbf{u}^*$ for which mass conservation is not necessarily realized, following:

$$\begin{aligned}\rho\frac{\mathbf{u}^* - \mathbf{u}^{(n)}}{\Delta t} &- \nabla\cdot\left((\rho\mathbf{u})^{(n)}\otimes\mathbf{u}^*\right) - \mathbf{u}^*\nabla\cdot\left((\rho\mathbf{u})^{(n)}\right)\\ &= -\nabla p^{(n)} - (\rho-\rho_{air})\mathbf{g}\\ &\quad + \nabla\cdot\left(\mu\left[\nabla\mathbf{u}^* + \nabla(\mathbf{u}^*)^T\right] - \frac{2}{3}\mu\nabla\cdot\mathbf{u}^*\,\mathbb{1}\right)\end{aligned} \tag{17}$$

where Δt is the fixed or varying time step size, $^{(n)}$ and $^{(n+1)}$ denote the previous and current time steps respectively. Note that ρ and μ are known at time (n) and will only be updated at the end of the time scheme loop, after the resolution of Eq. (16).

Correction step. In this step, the pressure increment $\delta p = p^{(n+1)} - p^{(n)}$ is computed to enforce mass conservation and thus correct $\mathbf{u}^*$ to yield the final field $\mathbf{u}^{(n+1)}$. Considering a form of Eq. (11) in which non-pressure right-hand side (RHS) terms are neglected, it becomes:

$$\frac{\mathbf{u}^{(n+1)} - \mathbf{u}^*}{\Delta t} = -\frac{1}{\rho}\nabla\delta p \tag{18}$$

$$\nabla\cdot\mathbf{u}^{(n+1)} = 0. \tag{19}$$

Taking the divergence of Eq. (18) and using Eq. (19) leads to the following Poisson equation:

$$\nabla\cdot\mathbf{u}^* = \nabla\cdot\left(\frac{\Delta t}{\rho}\nabla\delta p\right) \tag{20}$$

from which $p^{(n+1)}$ then $\mathbf{u}^{(n+1)}$ are deduced.

Time integration of the scalar transport equation. The last step in the time-stepping procedure consists in the time integration of the scalar transport equation on α. To that end, an Implicit Euler scheme is selected.

$$\frac{\alpha^{(n+1)} - \alpha^{(n)}}{\Delta t} + \nabla\cdot(\alpha\mathbf{u})^{(n+1)} = 0 \tag{21}$$

With $\alpha^{(n+1)}$ available, it is then possible to get updated fluid properties $\rho^{(n+1)}$ and $\mu^{(n+1)}$ as well as mass fluxes $(\rho\mathbf{u})^{(n+1)}$ that are ready to be used in the next time step.

To compute the advection term of Eq. (21), various schemes might be selected in *CS*, namely the *Switching Technique for Advection and Capturing of Surfaces* (STACS, Darwish and Moukalled, 2006), the modified-*High Resolution Interface Capturing scheme* (M-HRIC, Muzaferija, 1999) and the modified-*Compressive Interface Capturing Scheme for Arbitrary Meshes* (M-CICSAM, Zhang et al., 2014).

All of them rely on the principle of blending a very compressive scheme and a high-resolution diffusive scheme, based on a weighting factor that is a function of the Courant number and other local conditions. The idea is to keep α from taking unphysical values outside of the range $[0;1]$ while also limiting interface diffusion.

In the current study, a version of the M-CICSAM scheme of Zhang et al. (2014) is used. Boundary conditions needed to fulfill time integration are described in detail in Archambeau et al. (2004).

4. Two-way coupling on overlapping subdomains

In this work we chose to implement a NT coupling, given that resolving the Bernoulli equation for the velocity potential on *seine3d*'s coupled boundary is not needed, hence making implementation easier, and as higher stability of the NT coupling as compared to DT was reported by Colicchio et al. (2006). Potential and viscous domains are coupled through the mutual exchange of computational variables at their coupled boundaries.

Velocity and free surface position are the exchanged physical variables, but it should be noted that the latter is not a direct outcome of a NS-VOF simulation, where a free surface capturing scheme is used. By contrast, the free surface geometry is explicitly known in the potential code. Raw coupling information extracted from one model should thus be processed and adapted to the other model's requirements prior to being used in the coupling procedure, as both models employ different spatial and temporal discretizations, as well as different representations of the free surface.

Certain *CS* computational fields (air fraction and /or velocity) may also optionally be modified in the computational volume as well, through source terms added to the governing equations, based on values extracted in the interior of *seine3d*'s domain. These optional source terms were not found necessary to the accuracy and stability of hybrid computations, therefore they are not further mentioned in the description of the coupling strategy. However, as they are needed for wave generation and damping in *CS*-only simulations, a description is given in Section 5.3.1 in this context.

4.1. Overlapping subdomains

A coupling strategy requiring BEM and VOF domains to partially overlap is employed in this study, as illustrated in Fig. 1. The associated overlapping region $\Omega_{overlap}$ is bounded by coupling boundaries $\Gamma^{\mathrm{D}}_{\mathrm{c,CS}}$ and $\Gamma^{\mathrm{N}}_{\mathrm{c},seine3d}$ with D standing for a Dirichlet boundary condition on water velocity on *CS* side and N for a Neumann boundary condition on the velocity potential on *seine3d* side. $\Gamma_{fc,seine3d}$ is the part of $\Gamma_{f,seine3d}$ that receives a free surface position signal from *CS* during the coupling process. Coupling boundary conditions for this type of coupling are recalled in the following system and are described in detail in the next sections.

$$\mathbf{u}_{\mathrm{CS}} = \mathbf{u}_{seine3d} \qquad \text{at } x = x_{\mathrm{CS}} \tag{22}$$

$$\mathbf{u}_{\mathrm{CS}}\cdot\mathbf{n}_{seine3d} = \frac{\partial\phi}{\partial n} \qquad \text{at } x = x_{seine3d} \tag{23}$$

where x_{CS} and $x_{seine3d}$ designate the location of both ends of the overlapping region.

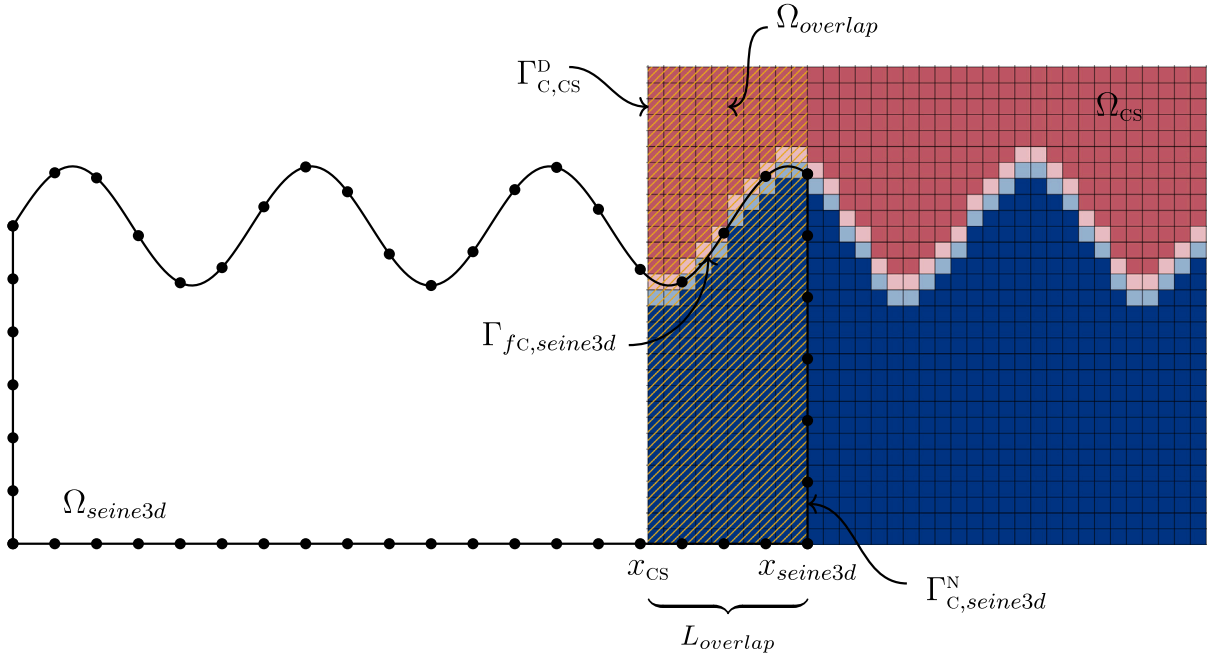

Fig. 1. Coupled domains and related boundaries. Blue *CS* cells are cells filled with water, while red cells are full of air. Pale blue and pale red cells contain a mix of the two phases.

4.2. Velocity matching at coupled boundaries

4.2.1. Wave generation in the VOF model

In the collocated finite volume formulation of *CS*, boundary conditions are needed at the centers of boundary faces. Let $\Gamma^{\mathrm{D}}_{\mathrm{C,CS}}$ represent the set of boundary faces involved in the coupling. With the *CS* mesh fixed, boundary face center coordinates are extracted once at the beginning of a calculation and sent to the coupled *seine3d* instance. Elements involved in the construction of this boundary condition are recalled in Fig. 2. At each *CS* iteration, water velocity and air fraction boundary conditions on $\Gamma^{\mathrm{D}}_{\mathrm{C,CS}}$ are generated from the variables $\mathbf{u}_{seine3d}$ and $\eta_{seine3d}$ sent by *seine3d* (Algorithm 1). $\Gamma^{\mathrm{D}}_{\mathrm{C,CS}}$ boundary surface is then split into two parts, each one corresponding to a given phase of the fluid and receiving its own set of boundary conditions. A Dirichlet boundary condition on the air fraction is employed in both phases to set the free surface vertical position. A linear approximation is applied in the case of a cell intersecting the free surface position. Free surface in the cell is, to a first approximation, horizontal, hence the volume of water in the cell and thus the air fraction value can be deduced from the distance from the cell floor to $\eta_{seine3d}$ if the latter is above the cell center in the case of a cell mostly filled with air or from the ceiling if the cell is mostly filled with water. A Dirichlet boundary condition on all velocity components in the water phase is used to generate waves in this study, as in a number of other VOF models. The boundary value problem would not be complete without a condition on pressure. A homogeneous Neumann boundary condition on pressure is used in either part of $\Gamma^{\mathrm{D}}_{\mathrm{C,CS}}$, i.e., a zero normal pressure gradient is imposed (which is the default for pressure in the *Inlet* and *Symmetry* conditions of *CS*).

The process is summarized for coupled variables in the following algorithm, where i stands for the *CS* coupled boundary face of interest, for which $\eta_{seine3d,i}$ is the vertical position of the free surface. $z_{i,cen.}$ is the adjacent cell center vertical coordinate.

The boundary condition for velocity in the part of $\Gamma^{\mathrm{D}}_{\mathrm{C,CS}}$ that lies in the air phase can be imposed in different ways, but the velocity field in the air phase is not of direct interest in these simulations, at least in the outer region of the *CS* domain. It is therefore not mandatory to impose a realistic vertical velocity profile at the edge of the domain. Using a free-slip (i.e., *symmetry*) boundary condition assigns a zero Dirichlet condition on the velocity component normal to the face and a homogeneous Neumann condition on its tangential components.

Algorithm 1 Dirichlet velocity and air fraction boundary condition on $\Gamma^{\mathrm{D}}_{\mathrm{C,CS}}$.

for $i = 1$ to $card\left(\Gamma^{\mathrm{D}}_{\mathrm{C,CS}}\right)$ **do**
  if $z_{i,cen.} \leq \eta_{seine3d}$ **then**
    if $z_{i,cen.} \geq \eta_{seine3d} - \frac{dz}{2}$ **then**
      $\alpha_i \leftarrow \frac{z_{i,cen.} + \frac{dz}{2} - \eta_{seine3d}}{dz}$
    else
      $\alpha_i \leftarrow 0.0$
    end if
    $\mathbf{u}_i \leftarrow \mathbf{u}_{seine3d}(z = z_{i,cen.})$
  else
    Set velocity and air fraction boundary conditions for air phase
  end if
end for

4.3. Velocity in the interior of NWT domain

The velocity computation in the interior of the NWT domain is, similar to Eq. (3), computed by another integral:

$$\mathbf{u}_{seine3d} = \nabla\phi(\mathbf{x}_i) = \int_{\Gamma}\left[\frac{\partial\phi}{\partial n}(\mathbf{x})Q - \phi(\mathbf{x})\frac{\partial Q}{\partial n}\right]\mathrm{d}\Gamma, \tag{24}$$

with gradient of the Green's function given as:

$$Q(\mathbf{x}-\mathbf{x}_i) = \frac{(\mathbf{x}-\mathbf{x}_i)}{4\pi\, r_i^3} \tag{25}$$

$$\frac{\partial Q}{\partial n}(\mathbf{x}-\mathbf{x}_i) = \frac{1}{4\pi\, r_i^3}\left[\mathbf{n} - 3((\mathbf{x}-\mathbf{x}_i)\cdot\mathbf{n})\frac{\mathbf{x}-\mathbf{x}_i}{r_i^2}\right] \tag{26}$$

and which is further described in Fochesato et al. (2005). Using numerical quadrature for Eq. (24) can be prone to instabilities for points near any *CS* boundary due to the singular integrals. If the free surface

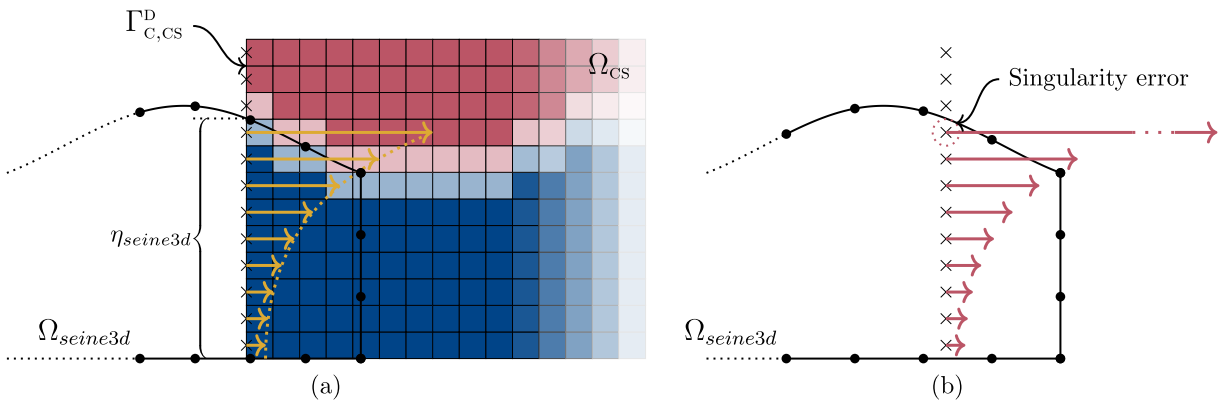

Fig. 2. Velocity field considered at the *CS* coupled boundary, with crosses marking the centers of the boundary faces belonging to $\Gamma^{D}_{C,CS}$ where the velocity is sought in *CS*: (a) yellow arrows represent the corrected vertical profile of the horizontal velocity $\mathbf{u}_{seine3d}$; (b) calculation of the horizontal internal velocity close to the free surface in *seine3d* domain, with red arrows representing the partially unphysical vertical velocity profile of $u_{seine3d}$ while dashed ones (as shown in panel (a)) illustrate the corrected velocity profile (by local extrapolation).

boundary $\Gamma_{f,seine3d}$ comes too close to a *CS* boundary face center belonging to $\Gamma^{D}_{C,CS}$ where the *seine3d* interior velocity is sought, erroneous value is sent to *CS* as a boundary condition in the current iteration of the coupling, and the simulation may diverge and fail. As *CS* boundary face centers are supposed to be aligned along vertical lines in a dense pattern – typically 20 cells or more per wave height – compared to the number of *seine3d* elements in a vertical, this situation happens frequently during a simulation. Though treatments of singularities by methods such as PART of Hayami and Matsumoto (1994) could solve this problem, a simple but efficient approach based on extrapolation is used here. It is then necessary to set a threshold value in *seine3d* for one or for all of the components of the internal velocity vector above which velocity is recalculated by extrapolation from values at underlying *CS* face centers. A corrected velocity value is then sent to *CS*.

To extrapolate a value along the vertical, a polynomial is established using a least-squares fit to the velocity values at underlying internal basis points that is later used for extrapolation. Such extrapolation is done on all velocity components. It is to be noted that this one-dimensional extrapolation strategy is valid only in the case of a *CS* mesh whose face centers are aligned along verticals. In the most general 3D case, such a mesh could be built from the (possibly non-uniform) vertical extrusion of an arbitrary conformal horizontal 2D mesh. *CS* meshes used for coupling should therefore comply with the latter rules. Fig. 2b illustrates this upwards extrapolation process in the case of an horizontal internal velocity field featuring spurious values close to the free surface.

The same type of error occurs for a *CS* boundary face center from $\Gamma^{D}_{C,CS}$ located too close to the *seine3d* domain bottom, in which case a similar but downwards extrapolation strategy is employed. While these precautions are sufficient for 2D simulations, this is not the case in 3D. Indeed, it appeared that in this latter case some coupled *CS* boundary face centers may lie too close to the *seine3d* lateral vertical boundaries, leading to the same type of errors. It was then decided in this case to employ a simpler "nearest neighbor" extrapolation method for which the replacement velocity value is chosen from the closest interior point of *seine3d* with a velocity norm lower than the above-mentioned threshold value.

Singularity errors related to velocity extraction in the interior of *seine3d* may also partially be treated from the tuning of some numerical parameters of *seine3d*. This model can indeed solve certain singularity problems with subdivisions of boundary elements allowing adaptive integration of the BIE kernel. The higher the number of subdivisions allowed to handle singularities, the closer to *seine3d* boundaries the coupled *CS* boundary face centers may lie without any divergence of the extracted coupling velocity values. This reduces the need for the aforementioned extrapolation schemes, but at the cost of increased simulation times for *seine3d* and therefore for the coupled simulations as adaptive integration is time-consuming. A trade-off between accuracy and speed should then be sought so that subdivisions are used efficiently. Here a maximum of four subdivisions were considered for points near a boundary. Details of this algorithm can be seen in Harris et al. (2022).

4.4. Velocity extraction in CS domain

In this Neumann-type coupling methodology, *CS* produces a value for the normal derivative of the velocity potential $\frac{\partial \phi}{\partial n}$ on the lateral coupling boundary $\Gamma^{N}_{C,seine3d}$. As the physical assumptions made in *seine3d* are more stringent than those applying in *CS*, one should make sure that the *seine3d* constraints of irrotational flow, negligible viscous effects and single-valued free surface are valid in the overlapping region. This predicament governs the location and horizontal extension of $\Omega_{overlap}$. Assuming these requirements are met, we can admit that the *CS* velocity known at the location of a *seine3d* boundary node is that of a potential flow. Its projection along the normal direction to the local BEM element produces a Neumann boundary condition on the potential.

The *seine3d* surface mesh moves with the fluid in a semi-Lagrangian fashion. Thus, contrary to *CS* boundary face centers belonging to $\Gamma^{D}_{C,CS}$ where *seine3d* velocity is calculated and whose position is fixed and known at the beginning of the simulation, velocity extraction in *CS* is done in locations varying with time. This poses issues of computational cost to the coupling algorithm if not implemented adequately. However, cell selection based on geometrical criteria is easily realized in *CS* and is described in Fig. 3.

An array containing the coordinates of all the coupled *seine3d* nodes is sent to *CS* at every iteration of the coupling. A box of constant dimensions is built in the *CS* domain around each *seine3d* node, the latter coinciding with the geometrical center of the box. Cells with a center inside the box are selected, and the associated velocity $\mathbf{u}_{CS}$ values, stored at cell centers, are saved, along with cell center coordinates. There may be several selected cells for each *seine3d* node, and multiple *seine3d* nodes associated to the same *CS* cell in the case of 2D vertical simulations. Indeed, we place multiple nodes in the width of a *seine3d* domain even for two-dimensional calculations, whereas one cell occupying the entire width is sufficient for *CS* in that case.

Because of the absence of a bijection between *seine3d* nodes and *CS* cells, and because *CS* cell extraction functions do not preserve cell order, arrays containing *CS* cell center coordinates and corresponding velocity values are sent back to *seine3d* in arbitrary order of the cells. It is to be noted that in the current state of the coupling methodology, no gradient calculation is conducted for coupled velocity extracted

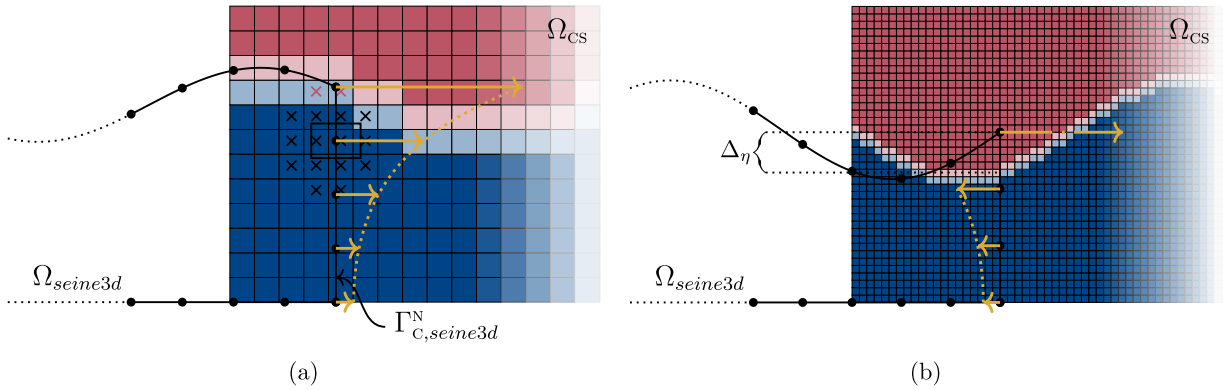

Fig. 3. Boundary condition on the velocity potential for the *seine3d* in the overlapping region, with crosses marking the centers of *CS* cells in the vicinity of a given *seine3d* node. *CS* cells too close to the free surface to yield a correct velocity value bear red crosses and a rectangle stands for the selection box centered on the *seine3d* node: (a) interpolation scheme for matching conditions; (b) demonstration of mismatch of the vertical profile of normal velocity, in yellow ($\mathbf{u}_{seine3d} \cdot \mathbf{n}$).

from *CS*. Then, for every coupled *seine3d* node, the distance to every extracted *CS* cell center is computed, and $\mathbf{u}_{CS}$ is taken as the value at the closest cell center. Such nearest neighbor approximation scheme is first-order accurate in *CS* mesh cell size. This sorting operation is realized in a single MPI process of *seine3d* (the one with root rank), so it is a blocking step for the simulation and its cost is therefore not negligible. Selecting the lowest possible number of *CS* cells using the smallest selection box is then of central interest. In practice, the choice of the selection box size is left to the user, and it is straightforward in the case of a uniform Cartesian grid, for which the box should be slightly larger than a cell so that *CS* cells are always located.

VOF models are also known to suffer from the occurrence of spurious velocities close to the free surface. Therefore, if a coupled *seine3d* node lies in the area of mixed phases in *CS* domain, as illustrated by the red crosses in Fig. 3, the velocity extracted near its location may be nonphysical. If this is the case, this will surely lead to the failure of the simulation. To avoid such an issue, velocity is not extracted in the region of mixed phases, but a large dummy value is rather sent to *seine3d*. Unless stated otherwise, this was taken to be all points within $3\Delta z$, but early tests showed that this value depends on the selected air fraction advection scheme so may need to be modified if adapted for other NS solvers. In turn, when *seine3d* receives such a dummy value, a vertical extrapolation procedure similar to that used for the internal velocity transmitted to *CS* is conducted. Basis points then needed for a second-order polynomial regression are *seine3d* nodes belonging to $\Gamma^{N}_{C,seine3d}$ and located beneath the current node. Algorithm 2 summarizes the procedure. *threshold* value is only used to detect large dummy values requiring local extrapolation. Once $\mathbf{u}_{CS}$ is known at all nodes located on $\Gamma^{N}_{C,seine3d}$, it is projected on the local normal vector to generate a Neumann boundary condition on the potential.

Algorithm 2 Neumann boundary condition on $\Gamma^{N}_{C,seine3d}$.

1: **for** $i = 1$ to $card\left(\Gamma^{N}_{C,seine3d}\right)$ **do**
2: Calculate distances from the current node to every extracted CS cell center
3: Get closest CS cell center and associated $\mathbf{u}_{CS,i}$
4: **if** $\mathbf{u}_{CS,i} > threshold$ **then**
5: Extrapolate velocity from underlying nodes
6: **end if**
7: $\left(\frac{\partial \phi}{\partial n}\right)_i \leftarrow \mathbf{u}_{CS,i} \cdot \mathbf{n}_i$
8: **end for**

4.5. Free surface matching in the overlapping region

4.5.1. A need for matching free surfaces in $\Omega_{overlap}$

The velocity exchange procedure described above does not guarantee the matching of free surfaces in $\Omega_{overlap}$. On the *CS* side of the overlapping region, free surface information on $\Gamma^{D}_{C,CS}$ is received from *seine3d* along with velocity data as the velocity profile imposed to the water phase on the boundary is of limited vertical extent. On the opposite, velocity extraction in *CS* cells located near $\Gamma^{N}_{C,seine3d}$ nodes does not incorporate any free surface position information, and velocity values are sought in the *CS* domain without any restriction on the phase in which extraction is realized. An additional operation on the free surface of *seine3d* is then needed to ensure interface continuity between the viscous and potential domains, which was found to be a necessary condition for the accuracy and stability of coupled simulations.

If free surface positions $\eta_{CS}(\mathbf{x}_{CS})$ and $\eta_{seine3d}(\mathbf{x}_{CS})$ differ on the *CS* side of $\Omega_{overlap}$, the *seine3d* vertical velocity profile specified on $\Gamma^{D}_{C,CS}$ does not match the geometry of the water phase in the interior of the *CS* domain. As the imposition of this velocity profile comes along with that of a Dirichlet boundary condition on the air fraction on $\Gamma^{D}_{C,CS}$ as described in 4.2.1, free surface mismatching leads to an artificial jump in the air fraction field, either positive or negative, causing a spurious free surface flow. Such an air fraction jump and subsequent gravity-driven flow deteriorate the accuracy of simulations but were found seldom problematic for their stability in preliminary tests.

Conversely, a free surface mismatch on the *seine3d* side of the overlapping region quickly produces a growing instability in *seine3d*. Coupled nodes belonging to $\Gamma^{N}_{C,seine3d}$ may happen to be located in the air phase of the viscous domain, or at least in the area of mixed phases. Because of the incompressible nature of the flow simulated with the VOF method, and due to the high-density ratio between phases, the velocity in the air phase may be several orders of magnitude higher than in the dense phase. If a *seine3d* node where normal velocity is needed is located in the air phase, the velocity value it gets from *CS* can largely exceed velocity values in the rest of the potential domain, leading to a divergence in the resolution of the Laplace equation and consequently to the failure of the calculation in *seine3d*. If the same node lies in the region of mixed phases near the free surface, the velocity may still take spurious values – which are common in VOF simulations – triggering the same type of instability.

One thus has to make sure that the free surface position in *seine3d* and the air fraction field in *CS* remain consistent in the overlapping region, with a special focus near the endpoint of each domain. It appears that no special treatment is necessary on the *CS* side of $\Omega_{overlap}$ and that the air fraction jump can be avoided with a cautious selection of the coupling parameters that will be presented in the coming sections. The interface position in *seine3d*, on the contrary, has to be relaxed towards the estimated location of the interface in *CS* over the whole extent of the overlapping region.

4.5.2. Capturing the free surface in *CS*

As mentioned, the free surface position is not explicitly known in simulations conducted with the algebraic VOF module of *CS*. The

region of mixed phases around the free surface is smeared over a few cells even with the use of an interface recompression method. Taking advantage of the fact that the free surface topology in the overlapping area satisfies assumptions made in *seine3d*, in particular it has to be single-valued, a method to estimate the vertical position of the free surface in *CS* is devised. For every coupled *seine3d* node where the free surface vertical position is sought in *CS*, we consider the complete fluid column extending vertically from the position of the associated *CS* cell, whose center is the closest to the *seine3d* node of interest. The free surface vertical location $z_{fc,\mathrm{cs}}$ is approximated by the ratio of the water volume in the column to the total volume of the column. Computing volumes by vertical integration gives:

$$\eta_{\mathrm{cs}} = \frac{\int_{-h}^{h_c}(1-\alpha)d\Omega}{\int_{-h}^{h_c} d\Omega} \tag{27}$$

where α is the air fraction, h is the depth, h_c the height of the *CS* domain above the resting free surface (up to the ceiling) and $d\Omega$ is an infinitesimal volume.

As the meshes used for coupled simulations in *CS* are structured in the vertical direction, i.e., they can be obtained from the vertical extrusion of an arbitrary horizontal 2D conformal mesh, a column of cells is also a fluid column. Calculation of water volume and total column volume is then straightforward and Eq. (27) becomes:

$$\eta_{\mathrm{cs}} = \frac{\sum_{j\in C_i}(1-\alpha_j)|\Omega_j|}{\sum_{j\in C_i}|\Omega_j|} \tag{28}$$

for every cell j of volume $|\Omega_j|$ in the fluid column C_i centered on cell i. This way η_{cs} can take any value within the continuous range $[-h; h_c]$.

4.5.3. Free surface relaxation in *seine3d*

Principle of free surface relaxation. $\Gamma_{fc,seine3d}$ is modified to conform with the free surface solution η_{cs} in $\Omega_{overlap}$ built in *CS* as described in Section 4.5.2 (see Fig. 1). Time-stepping in *seine3d* follows a semi-Lagrangian rule, thus only the vertical coordinate of the *seine3d* nodes belonging to $\Omega_{overlap}$ is modified. Relaxation refers to the fact that the pure potential free surface solution which has just been computed in *seine3d* is combined with a free surface signal extracted from the *CS* air fraction field at the same time instant to produce a relaxed solution. This ensures free surface matching at the *seine3d* side of the overlapping region at any time. Following the time stepping stage in *seine3d*, the vertical position of each node i belonging to $\Gamma_{fc,seine3d}$ is replaced by the weighted sum of *seine3d* free surface position and *CS* free surface solution η_{cs}, as:

$$z \leftarrow (1-R)z + R\eta_{\mathrm{cs}} \qquad \text{on } \Gamma_{fc,seine3d}, \tag{29}$$

where z is the current vertical coordinate while ω is the relaxation weight, varying between 0 at $\mathbf{x}_{\mathrm{cs}}$ and 1 at $\mathbf{x}_{seine3d}$ over the length of $\Omega_{overlap}$. Different spatial functions may be used for ω to allow a smooth relaxation. The relaxation strategy is illustrated in Fig. 4, where a yellow line marks the corrected position of the free surface.

One drawback of this relaxation is that mass conservation is no longer ensured in the coupled *seine3d* domain, as an extra mass flux originates from the changes made to the interface geometry in $\Omega_{overlap}$. Its magnitude grows with the gap between the target value η_{cs} and the geometry of $\Gamma_{fc,seine3d}$ prior to relaxation. The accumulated errors might lead to the failure of the coupled simulation. To avoid this and to make sure that free surface boundary conditions are still satisfied after the interface relaxation step, the velocity potential on $\Gamma_{fc,seine3d}$ should be modified accordingly, as described in more detail in Section 4.6.4.

Relaxation weight. Different spatially varying functions, or blending functions, can be used for ω in Eq. (29), such as linear, exponential, or third-order polynomial. The associated weights are given hereafter, setting $b = \frac{x-x_{\mathrm{cs}}}{L_{overlap}}$ with x the current horizontal coordinate. Relaxation weights were based on third-order cubic polynomials:

$$R_{herm.} = b^2(3-2b) \tag{30}$$

though exponential variation has also been tested, the change in function seems to have no significant impact on the simulation results. A thorough comparison of the performance of blending functions was nevertheless not considered in this study.

Relaxation of the velocity potential on the free surface. As the position of free surface nodes is modified, so should be the value of the velocity potential ϕ at these nodes, as follows:

$$\phi \leftarrow (1-R)\phi + R\phi_{rlx} \qquad \text{on } \Gamma_{fc,seine3d} \tag{31}$$

The potential has no physical meaning in the NS simulation, thus its corrected value ϕ_{rlx} should be built from other *seine3d* and *CS* variables. Before explaining how ϕ_{rlx} is obtained, we should introduce the time-stepping strategy used for coupled simulations. This is the subject of the next section, in which ϕ_{rlx} is described.

4.6. Advancing coupled simulations in time

The extraction and processing of coupling variables as well as the imposition of coupling boundary conditions having been detailed in previous sections, we now explain how time stepping is done in coupled BEM-VOF simulations.

4.6.1. Using different time step sizes for each code

The time step size in each code is governed by physical and numerical considerations, but primarily through the Courant–Friedrichs–Lewy (CFL) number. Notably, spatial discretization differs significantly between *CS* and *seine3d*. While in the former a target number of 20 cells along the vertical direction is employed to cover the height of the reference wave, the latter only requires a smaller number (typically 4 or slightly more) of boundary elements to occupy the whole water column under the wave. The need for limited aspect ratios of *CS* cells, as well as *seine3d* boundary elements, further sets constraints on the number of cells or boundary elements per reference wavelength in each code. Such differences in spatial discretization call for the use of different time-step sizes, so that there is flexibility to set the CFL numbers in each code independently. Using *CS* and *seine3d* with respective sets of parameters close to optimal values is indeed a necessary condition for the global efficiency of the coupling strategy. As a result, the *CS* time step size Δt_{cs} has to be kept smaller than its potential counterpart $\Delta t_{seine3d}$. We define the time step ratio $N_{\Delta t}$ as:

$$N_{\Delta t} = \frac{\Delta t_{seine3d}}{\Delta t_{\mathrm{cs}}} \tag{32}$$

Both models are synchronized when the coupled computation time reaches an integer multiple of $\Delta t_{seine3d}$, that is to say that physical variables of interest are exchanged through MPI communications every $\Delta t_{seine3d}$ seconds. *seine3d* is thus waiting for *CS* calculations over sub time steps (of size Δt_{cs}) to end during most of the computational time.

4.6.2. Interpolation between time steps

CS boundary conditions are needed at time $t^{(n_{\mathrm{cs}})}$ to advance the NS solution up to $t^{(n_{\mathrm{cs}}+1)}$ where n_{cs} enumerates the *CS* time stepping sub-stages between successive synchronization time instants $t^{(n)}$ and $t^{(n+1)}$.

$$t^{(n_{\mathrm{cs}})} = t^{(n)} + n_{\mathrm{cs}}\Delta t_{\mathrm{cs}} \qquad \forall\, n_{\mathrm{cs}} \in \{0, N_{\Delta t}-1\} \tag{33}$$

$$t^{(n_{\mathrm{cs}})} = t^{(n+1)} \qquad \text{if } n_{\mathrm{cs}} = N_{\Delta t} \tag{34}$$

Inlet Dirichlet boundary conditions on velocity and air fraction on $\Gamma^{\mathrm{D}}_{\mathrm{c,cs}}$ are obtained from interpolations of $\mathbf{u}_{seine3d}$ and $\eta_{seine3d}$ between $t^{(n)}$ and $t^{(n+1)}$. $\mathbf{u}^{(n_{\mathrm{cs}})}_{seine3d}$ and $\eta^{(n_{\mathrm{cs}})}_{seine3d}$ stand for values interpolated at time $t^{(n_{\mathrm{cs}})}$.

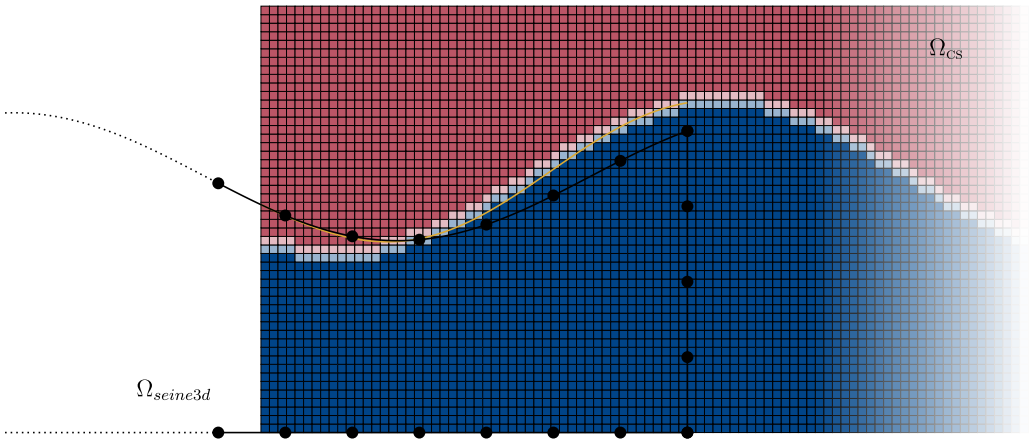

Fig. 4. Free surface relaxation in *seine3d*. The yellow line represents the position of *seine3d* free surface after correction.

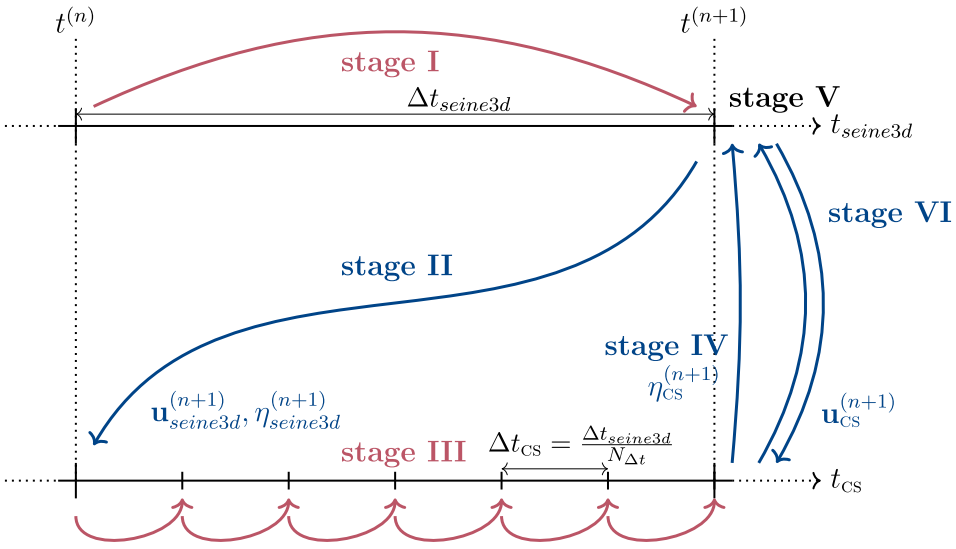

Fig. 5. Main stages and information fluxes of the coupling time-stepping scheme for marching from time $t^{(n)}$ to $t^{(n+1)} = t^{(n)} + \Delta t_{seine3d}$, with details of each stage given in Section 4.6.3. Red lines illustrate time-stepping operations while the blue ones show MPI communications between the coupled programs. The top axis stands for *seine3d* while the bottom axis represents the operations conducted in *CS*.

Interpolation schemes of various orders may be employed, using values of $\eta_{seine3d}$ and $\mathbf{u}_{seine3d}$ at different *seine3d* time instants.

If values of $\eta_{seine3d}$ and $\mathbf{u}_{seine3d}$ are stored at additional time instants $(n-1)$ and $(n-2)$, a higher-order interpolation procedure is established, permitting a better rendering of the nonlinear nature of the time evolution of wave kinematics. Such a scheme is more accurate than the linear one for a given time step size under certain assumptions, but it may lead to greater interpolation errors in the case of large time-steps. It also uses a larger amount of computer memory as physical variables are saved at four time instants, as opposed to two in the linear case. As constant time-step sizes are used exclusively in the coupling procedure, the Lagrange polynomial of the 3rd degree is retained that is easily implemented and expressed here in terms of the same variable β.

The number of coupling *seine3d* nodes being limited to relatively small values, storing *seine3d* coupling velocity profile and free surface function at 4 time instants is not very memory-consuming. Besides, $\Delta t_{seine3d}$ values were found to remain in a range where high-order polynomial interpolation is more accurate than the linear one. It is to be noted that the choice of $N_{\Delta t}$ is the result of a balance between accuracy (limited interpolation errors) and efficiency (sufficiently high CFL number in *seine3d*), and as such is a crucial parameter of the coupling strategy.

4.6.3. Detailed description of the time-stepping

The time-stepping procedure is summarized in the flow chart of Fig. 5, with roman figures enumerating the different stages, described below:

> **stage I**: the *seine3d* free surface conditions are advanced in time from $t^{(n)}$ to $t^{(n+1)}$ following the explicit 3^{rd}-order Runge–Kutta scheme described in Section 3.1.2. The geometry of the *seine3d* domain is updated, and so are $\Gamma_{\mathrm{c},seine3d}^{\mathrm{N},(n+1)}$ and $\Gamma_{fc,seine3d}^{(n+1)}$. To complement the set of boundary conditions of the potential problem at time $t^{(n+1)}$, a Neumann boundary condition on the velocity potential on $\Gamma_{\mathrm{c},seine3d}^{\mathrm{N},(n+1)}$ is built from a *CS* vertical velocity profile extracted at time step $t^{(n)}$:
>
> $$\frac{\partial \phi}{\partial n}^{(n+1)} = \mathbf{u}_{\mathrm{CS}}^{(n)} \cdot \mathbf{n}_{seine3d} \text{ on } \Gamma_{\mathrm{c},seine3d}^{\mathrm{N},(n+1)} \tag{35}$$

$\mathbf{u}_{\mathrm{CS}}^{(n)}$ is available as an output of the previous coupling iteration. It should be noted that the velocity profile $\mathbf{u}_{\mathrm{CS}}^{(n)}$ has been extracted (and is therefore known) at the previous location of the coupled *seine3d* nodes, i.e. on $\Gamma_{\mathrm{c},seine3d}^{\mathrm{N},(n)}$. We assume that this holds on $\Gamma_{\mathrm{c},seine3d}^{\mathrm{N},(n+1)}$. Then, the potential problem is solved at time $t^{(n+1)}$ by *seine3d*.

stage II: the internal velocity $\mathbf{u}_{seine3d}^{(n+1)}$ is extracted in the *seine3d* domain. Spurious velocity values are replaced with extrapolated ones, as explained in Section 4.3. Then, $\mathbf{u}_{seine3d}^{(n+1)}$ and $\eta_{seine3d}^{(n+1)}$ are sent to *CS* in an MPI communication operation.

stage III: the *CS* solution is advanced in time from $t^{(n)}$ to $t^{(n+1)}$ through $N_{\Delta t}$ sub time steps with the inlet boundary conditions described in Section 4.6.2.

stage IV: at time $t^{(n+1)}$, *CS* free surface data $\eta_{\mathrm{CS}}^{(n+1)}$ at cells close to free surface nodes belonging to $\Gamma_{fc,seine3d}$ is sent to *seine3d*.

stage V: the free surface position in *seine3d* is relaxed towards the *CS* solution, such that free surfaces matching is ensured at $x_{seine3d}$. Thus, $\Gamma_{\mathrm{c},seine3d}^{\mathrm{N},(n+1)}$ becomes $\Gamma_{\mathrm{c},seine3d}^{\mathrm{N},(n+1),rlx}$, and $\Gamma_{fc,seine3d}^{(n+1)}$ is now $\Gamma_{fc,seine3d}^{(n+1),rlx}$. The velocity potential can be relaxed accordingly, following the procedure explained in Section 4.5.3.

stage VI: the coordinates of *seine3d* boundary nodes on $\Gamma_{\mathrm{c},seine3d}^{\mathrm{N},(n+1),rlx}$ are sent to *CS*. The velocity $\mathbf{u}_{\mathrm{CS}}^{(n+1)}$ close to those nodes in *CS* domain is extracted and sent back to *seine3d* to generate an updated Neumann boundary condition at $t^{(n+1)}$ as follows:

$$\frac{\partial \phi}{\partial n}^{(n+1)} = \mathbf{u}_{\mathrm{CS}}^{(n+1)} \cdot \mathbf{n}_{seine3d} \quad \text{on } \Gamma_{\mathrm{c},seine3d}^{\mathrm{N},(n+1),rlx} \tag{36}$$

stage VII: in *seine3d*, the boundary integral problem at time $t^{(n+1)}$ is solved for the second time.

This two-way coupling strategy is similar to the one described in Kim et al. (2010) and theoretically enables wave propagation in any direction.

4.6.4. Calculation of ϕ_{rlx}

With the newly introduced time-stepping exponents, Eq. (29) can be written as:

$$z^{(n+1)} \leftarrow (1-R)z^{(n+1)} + \omega\eta_{\mathrm{CS}}^{(n+1)} \qquad \text{on } \Gamma_{fc,seine3d}^{(n+1)} \tag{37}$$

as $\Gamma_{fc,seine3d}^{(n+1)}$ is turned into $\Gamma_{fc,seine3d}^{(n+1),rlx}$. As stated in , potential relaxation through $\phi_{rlx}^{(n+1)}$ is needed so that the influence of the free surface relaxation on the potential distribution on *seine3d* boundaries can be applied. ϕ_{rlx} is sought at time $t^{(n+1)}$ and Eq. (31) becomes:

$$\phi^{(n+1)} \leftarrow (1-R)\phi^{(n+1)} + \omega\phi_{rlx}^{(n+1)} \qquad \text{on } \Gamma_{fc,seine3d}^{(n+1),rlx} \tag{38}$$

At stage *V* of the above coupling procedure, the dynamic free surface boundary condition is integrated again, this time in a single step and following a centered scheme:

$$\frac{\delta\phi}{\delta t}^{(n)} = \frac{\phi_{rlx}^{(n+1)} - \phi^{(n-1)}}{2\Delta t} \tag{39}$$

$$= -g\eta^{(n)} - \frac{1}{2}\left(\nabla\phi_{rlx}^{(n)}\right)^2 + \frac{\partial\eta_{rlx}^{(n)}}{\partial t}\frac{\partial\phi_{rlx}^{(n)}}{\partial z} \tag{40}$$

thus

$$\phi_{rlx}^{(n+1)} = \phi^{(n-1)} + 2\Delta t\left(-g\eta^{(n)} - \frac{1}{2}\left(\nabla\phi_{rlx}^{(n)}\right)^2 + \frac{\partial\eta_{rlx}}{\partial t}^{(n)}\frac{\partial\phi_{rlx}}{\partial z}^{(n)}\right) \text{ where } z = \eta(x,y,t^{(n)}) \tag{41}$$

Free surface velocity is rewritten as follows:

$$\nabla\phi_{rlx}^{(n)} = \nabla_h\phi^{(n)} + \frac{\partial\phi_{rlx}^{(n)}}{\partial z}\mathbf{e_z} \tag{42}$$

where ∇_h stands for the horizontal gradient and $\mathbf{e_z}$ is the vertical unit vector.

Every RHS term in Eq. (41) is known explicitly except $\frac{\partial\eta_{rlx}^{(n)}}{\partial t}$ and $\frac{\partial\phi_{rlx}^{(n)}}{\partial z}$. Using another centered scheme to solve the kinematic free surface boundary condition and obtain $\frac{\partial\eta_{rlx}}{\partial t}^{(n)}$, it becomes:

$$\frac{\partial\eta_{rlx}}{\partial t}^{(n)} = \frac{\delta\eta_{rlx}}{\delta t}^{(n)} = \frac{\eta_{\mathrm{CS}}^{(n+1)} - \eta^{(n-1)}}{2\Delta t} \tag{43}$$

$$= \frac{\partial\phi_{rlx}}{\partial z}^{(n)} - \frac{\partial\phi}{\partial x}^{(n)}\frac{\partial\eta}{\partial x}^{(n)} - \frac{\partial\phi}{\partial y}^{(n)}\frac{\partial\eta}{\partial y}^{(n)} \tag{44}$$

from which the value of $\frac{\partial\phi_{rlx}}{\partial z}^{(n)}$ is also deduced.

This method is inspired by that described in Kim et al. (2010) to relax the velocity potential on $\Gamma_{fc,seine3d}$. Other methods include not relaxing the free surface velocity potential, or using free surface velocity extracted in the viscous model to set the value of $\nabla\phi_{rlx}^{(n)}$, or that of its vertical component $\frac{\partial\phi_{rlx}^{(n)}}{\partial z}$ only, as in Kemper et al. (2019). In this latter work, the vertical velocity close to the interface extracted in the viscous code is used as vertical velocity at the free surface in the potential code. From time integration of the dynamic free surface boundary condition, a corrected value of the free surface potential is obtained. Free surface horizontal velocity in the VOF calculation is however not transmitted to the potential calculation. It is to be noted that extracting valid values for vertical water velocity in the viscous code at the free surface is not an easy task. It has been tested in the current coupled model but was found to be less accurate and stable than the above-described method.

4.7. Parallelization of coupled simulations

4.7.1. MPI communicator for coupling

Both potential and viscous numerical codes that are coupled in this work allow parallel simulations when used alone. They are adapted to high-performance computing on large computers with distributed memory, and coupled simulations should exhibit the same behavior. The Message Passing Interface (MPI) protocol is used with this goal in mind. Each application operates in a MPI communicator, or intracommunicator, allowing point-to-point and collective communications between processes owned by the application. In this case, allowing the exchange of variables between *CS* and *seine3d* amounts to building a new global communicator or extra-communicator from the union of both applications' communicators. This is done conveniently with ad-hoc MPI functions from the Parallel Location and Exchange (PLE) library (Fournier, 2020), coming with *CS*, that had to be adapted in *seine3d*. Exchanges of coupling variables are exclusively realized with point-to-point MPI communications in the newly built coupling (global) communicator. Such communications may be sequential if only root processes are involved, or parallel. Communicators and communications are illustrated in Fig. 6.

4.7.2. Sequential or parallel coupling communications

The choice between sequential or parallel coupling communications mostly depends on the characteristics of *CS* and *seine3d* and on the location of the variables of interest in the applications.

seine3d → *CS communications.* In *CS*, a domain decomposition approach is used to split the computational domain between MPI processes. Each process owns a part of the field variables arrays. Besides that, as the *CS* grid is fixed, the location of cells centers on $\Gamma_{\mathrm{c,CS}}^{\mathrm{D}}$, where the values of $\mathbf{u}_{seine3d}$ and $\eta_{seine3d}$ are sought, are known from the start of the simulation. Therefore, the *CS* processes that will receive these values from *seine3d* are identified at the initialization stage of the coupled calculation. Point-to-point communications are established between those *CS* processes and selected *seine3d* processes. Indeed the velocity at any internal point in $\Omega_{seine3d}$ and the position of any boundary free surface node belonging to $\Gamma_{fc,seine3d}$ may be respectively accessed or computed from any *seine3d* process. Coordinates of the

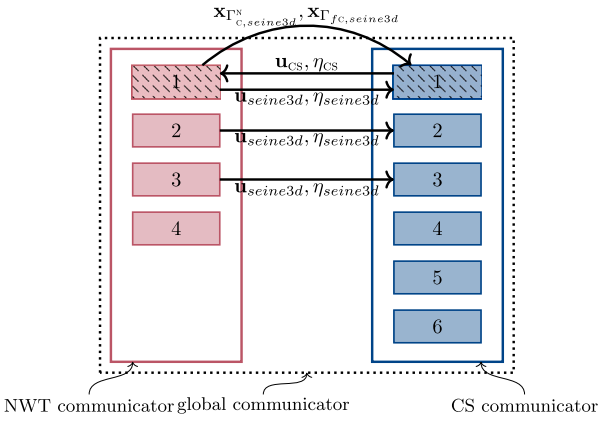

Fig. 6. MPI communicators and communications realized at each synchronized (*seine3d*) time step. Red boxes stand for *seine3d* processes while blue ones stand for *CS* processes. Hatched boxes represent root processes. Only processes with MPI ranks ranging from 1 to 3 are directly involved in the coupling. MPI communications at initialization are not shown for the sake of clarity.

above-listed coupled *CS* cell centers are then gathered at *CS*'s root process once and sent to *seine3d*'s root process, from where they are equally scattered to an arbitrary selection of *seine3d* processes and stored as internal points or used to create free surface gauges, allowing point-to-point MPI communications in parallel.

seine3d ← *CS communications.* As the grid of *seine3d* is moving, it is not possible to send the location of nodes where $\mathbf{u}_{\mathrm{CS}}$ and η_{CS} should be extracted to *CS* only once at the beginning of the simulation. This information is to be sent at every synchronization *seine3d* time step, after the free surface relaxation stage and before the second resolution of the boundary integral problem. *CS* cells extraction is explained in Section 4.4. Coupled *seine3d* node coordinates $\mathbf{x}_{\Gamma^{\mathrm{N}}_{c,seine3d}}$ and $\mathbf{x}_{\Gamma_{fc,seine3d}}$ are therefore gathered in *seine3d*'s root process and sent to *CS*'s root process, where they will be broadcast to every process. This is a sequential procedure, as only the root processes of the coupled applications are involved in MPI communications.

4.8. Coupling several instances of each code

So far, emphasis has been put on the most simple coupling case of one instance of *CS* and one instance of *seine3d*, in the context of 2D vertical applications. One of the goals of this study is to develop a flexible tool, adapted to a wide range of wave simulation applications. To that end, it was decided to allow the coupling of several instances of the applications. One *CS* application may indeed exchange simulation variables with several instances of *seine3d*, and the other way around. Currently accepted topologies include vertical lines, for 2D vertical couplings and vertical planes for 3D simulations.

Couplings are built as instances of C++ classes of *seine3d* and *C* structures of *CS*. It was intended to make the most of the object-oriented nature of *seine3d* to allow future improvements of the coupled model. In the following work and applications, we make extensive use of the coupling configuration *seine3d-CS-seine3d*, where the *CS* model is applied at a local scale around a marine structure.

5. Coupled 2DV regular waves simulation

5.1. General setup

The simulation of 2DV nonlinear regular waves is a natural and necessary step towards the calculation of 3D wave–structure interaction which is the final aim of this work. The experimental outputs of the WAS-XL (Wave loads and soil support for extra large monopiles) campaign Dadmarzi et al. (2019) are used as reference results for the computation of regular wave forces on a vertical cylinder representing a monopile OWT foundation. To set up the 2DV study detailed in the current section, we choose to use WAS-XL incoming waves parameters and domain geometry to validate the generation, propagation, transmission from one coupled domain to the other, absorption of periodic waves, and choose the spatial and temporal discretizations in both models, as well as those related to the coupling parameters $L_{overlap}$ (the length the of overlapping region) and $N_{\Delta t}$ (time step ratio), with the intention of reusing most of them for 3D studies in Section 6.

Table 1
Characteristics of simulated waves with steepness $\epsilon = 1/40$ and $h = 27$ m.

T (s)	λ (m)	H (m)	h/λ
9	114.45	2.86	0.236
12	171.37	4.28	0.158
15	226.67	5.75	0.119

As generation and absorption of regular waves are conducted in potential domains exclusively, correct absorption parameters in *seine3d* should be found before further tests. A quick analysis is realized and presented with this aim in mind. The nonlinear wave theory applied to generate waves is the so-called Stream-Function (SF) method, or more precisely the Fourier series approximation of the SF theory of Dean (1965), already implemented in *seine3d*. A depth-uniform horizontal current is added to the incident wave kinematics so that the net mass flux, averaged over a wave period, is zero, following Grilli and Horrillo (1997), removing the Stokes' drift. Most coupled simulation results presented in this section are conducted with the lowest wave steepness $\epsilon = H/\lambda = 1/40 = 2.5\%$ encountered in Dadmarzi et al. (2019), where H and λ are wave height and length respectively (Table 1). Such a definition of wave steepness slightly differs from the one used in Dadmarzi et al. (2019). In the WAS-XL campaign, steepness is defined as first-order wave height divided by wavelength. It seems that the use of such a definition involving the first-order wave height and not the total wave height has to do with constraints related to the wave-making device employed in the wave basin. In Dadmarzi et al. (2019) however, it is stated that a second-order correction of the piston motion is applied, to better account for the nonlinearity of the generated wave.

In the current coupled methodology, fully-nonlinear wave kinematics are imposed at the inlet boundary of the *seine3d* upstream domain as a Neumann condition (i.e., $\partial\phi/\partial x = u_{input}$) to generate waves, therefore steepness is computed as $\epsilon = H/\lambda$. Note that the simulated waves all belong to the intermediate depth regime, with $1/20 < h/\lambda < 1/2$. This 2DV study also serves the goal of determining the hybrid model limits, in particular in terms of wave steepness, so some results with the highest steepness used in Dadmarzi et al. (2019) ($\epsilon = 1/22 \approx 4.5\%$) are also presented.

5.1.1. Design waves from the WAS-XL campaign

To begin with, numerical simulations are set with the lowest depth value of 27 m and the smallest steepness $\epsilon = 1/40$. Wave height and length are specified following the above-mentioned SF algorithm of Dean (1965), in which no closed-form relation exists to link these two parameters. We then try a few subsequent combinations of wave height and length to roughly converge toward the desired steepness value, following a trial-and-error approach. Numerical results are obtained at full scale, while a 1:50 Froude scaling is selected for the models used in wave basin tests. Three wave periods of 9, 12, and 15 s are chosen that cover most of the range of the experimental wave periods, ranging from 6 to 16.5 s in Dadmarzi et al. (2019).

5.1.2. Numerical domains

The hybrid numerical domain employed for the coupled simulations is depicted in Fig. 7. It is essentially a projection of the 3D domain featuring the monopile on a vertical plane. In the WAS-XL experimental

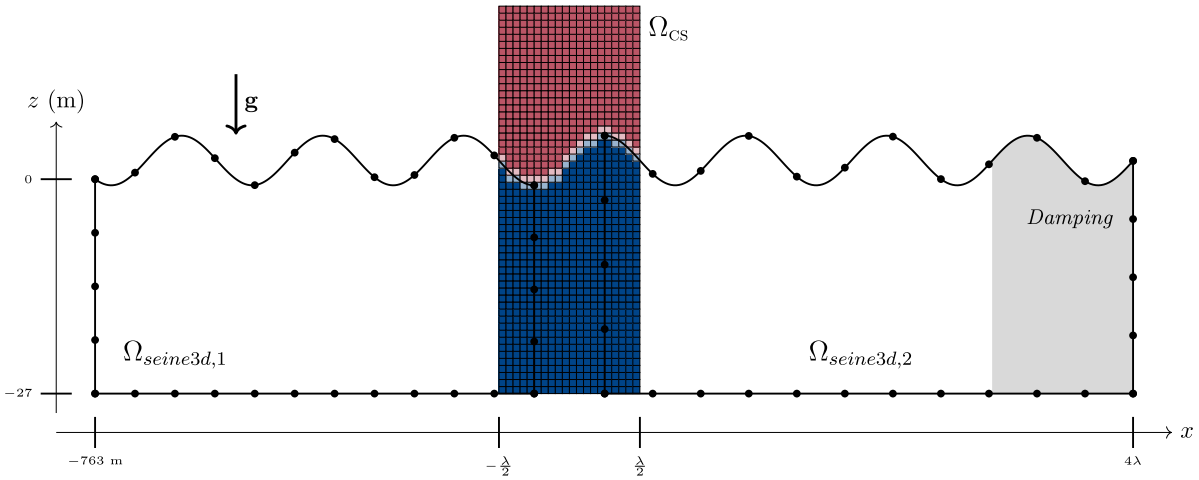

Fig. 7. Coupled domains for periodic wave simulations. Blue *CS* cells are cells filled with water, while red cells are full of air. Pale blue and pale red cells contain a mix of the two phases. *CS* mesh and *seine3d* boundary elements are drawn for illustrative purposes only. Horizontal proportions are realistic and correspond to the case of $T = 15$ s. The area in shaded gray represents the damping region in $\Omega_{seine3d,2}$, one wavelength long (given in Table 1).

setup, the distance between the monopile located at $x = 0$ m and the wave generation side is specified at $x = -763$ m. Thus this fixed-length upstream generation and propagation region represents a variable number of wavelengths, depending on the wave period considered. For the longest wave with $T = 15$ s (illustrated in Fig. 7), it still amounts to more than 3 wavelengths, which is sufficient to accurately generate waves in the potential domain *seine3d* 1. As can also be seen in the figure, the upstream region is mainly occupied by the *seine3d* 1 domain, the *CS* domain being restricted to one wavelength centered on $x = 0$ m.

Similarly, the distance from the monopile to the beginning of the absorbing beach is set to 3 wavelengths, large enough to propagate and absorb waves – mainly in the potential domain *seine3d* 2 – with limited spurious interactions in 3D simulations between wave diffraction by the vertical cylinder and possible wave reflections on the downstream boundary of the domain *seine3d* 2. As stated below, a one wavelength-long region at the downstream tip of the *seine3d* 2 domain is used to absorb waves going out of the domain, so a distance of 3λ is dedicated to wave propagation downstream of the virtual position of the cylinder.

5.2. Parameter choice in *seine3d*

Before applying the coupling methodology to simulate regular waves, it is necessary to ensure that *seine3d* alone can generate, propagate, and absorb traveling waves. The code should also prove capable of providing correct vertical profiles of velocity, thus anticipating their transmission to a *CS* instance.

5.2.1. Wave damping in *seine3d*

The major aspects of the wave-damping strategy are described in this section. The calculation of the reflection rate of the damping region is then explained, and an attempt is made to minimize it.

Numerical damping strategy. The damping device made of a parabolic absorbing beach associated with wave dampers in the tank facility is numerically recreated in the downstream potential domain *seine3d* 2 with the help of a damping region. It is based on ad-hoc terms D_η and D_ϕ added to the RHS of Eq. (8) and (9), as presented in Section 3.1. As the time-marching strategy selected in *seine3d* is explicit, the damping terms are built from geometrical and kinematic values at current (n) time instant. The damping terms are then:

$$D_\eta = -\gamma_{abs}(z - \eta_{ref}(\mathbf{x}))\left(\frac{x - x_{abs}}{L_{abs}}\right)^2 \qquad \text{if } x > x_{abs} \tag{45}$$

$$D_\phi = -\gamma_{abs}(w - w_{ref}(\mathbf{x}))\left(\frac{x - x_{abs}}{L_{abs}}\right)^2 \qquad \text{if } x > x_{abs} \tag{46}$$

where x and z are the coordinates of any *seine3d* free surface node whose position vector is $\mathbf{x}$ and whose vertical velocity is w. $\eta_{ref}(\mathbf{x})$ and $w_{ref}(\mathbf{x})$ stand for reference values towards which the vertical position and velocity of the free surface nodes are forced. In the case of a damping region, these values are those of the static solution for the undisturbed free surface:

$$\eta_{ref} = 0 \tag{47}$$

$$w_{ref} = 0 \tag{48}$$

and x_{abs} and L_{abs} are the starting abscissa and horizontal extent of the damping region respectively. A quadratic progression of D_η and D_ϕ on x is used, where γ_{abs} is the damping strength or damping intensity. If the same numerical value is used for γ_{abs} in both damping terms, physical dimensions differ. Rigorously speaking, two different variables should be employed, namely $\gamma_{abs,\eta}$ and $\gamma_{abs,\phi}$, with s^{-1} and $\mathrm{s}^{-1}\mathrm{m}^{-1}$ as respective units. To simplify the sensitivity analysis presented later, as already mentioned, it was quite arbitrarily decided to test the influence of a unique numerical value attributed to both $\gamma_{abs,\eta}$ and $\gamma_{abs,\phi}$. For this reason, and for the sake of brevity, the damping intensity is simply referred to as γ_{abs}, without any specification of units nor distinction between the associated free surface boundary equations.

γ_{abs} and L_{abs} are case-specific, and it is also expected that their values are somewhat related, as the damping intensity needed to absorb a given wave may not be independent of the distance over which absorption is realized. As in many wave simulation studies conducted with different physical assumptions and numerical solvers a length of $L_{abs} = \lambda$ is often used. This choice is repeated in the current work, bearing in mind that it is mostly arbitrary. Indeed, although it seems to be a suitable value, no sensitivity analysis related to L_{abs} and assessing the quality of the wave damping was made due to time constraints. For an in-depth description of the wave absorption strategy, the reader is referred to Grilli and Horrillo (1997).

The same cannot be said of γ_{abs}, whose value is modified to minimize wave reflection on the absorbing region. A quick and non-exhaustive study on the influence of γ_{abs} on the reflection coefficient R associated with the damping region is thus realized. The method used to compute this coefficient is that of Goda and Suzuki (1976), based on time-series from two wave gauges.

Application to the wave with $T = 15$ s. A 5λ-long *seine3d* domain is used to find a value of γ_{abs} minimizing the reflection induced by the damping layer, in the case of a wave with $T = 15$ s and $H = 5.75$ m,

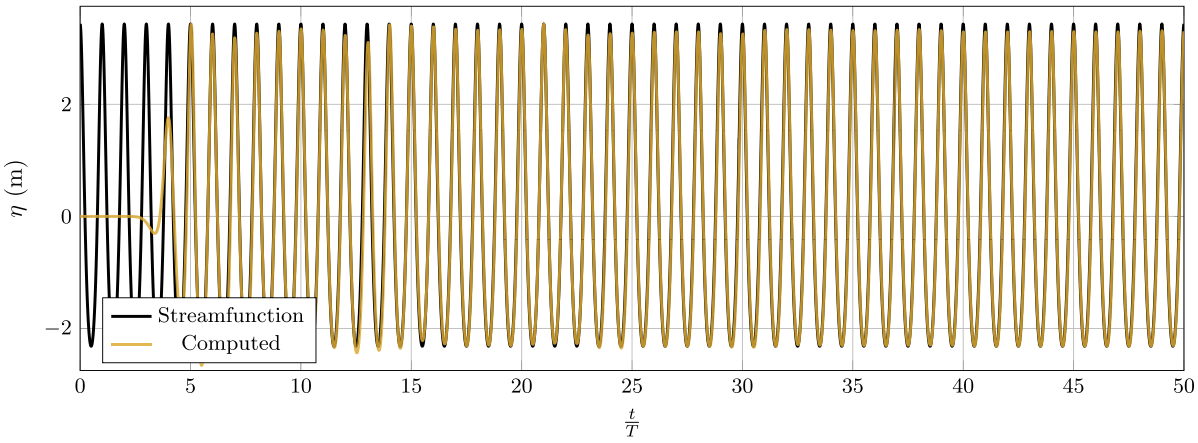

Fig. 8. Comparison of the SF and computed free surface signals at upstream wave gauge ($x_1 = 3\lambda$) used for the calculation of reflection coefficient.

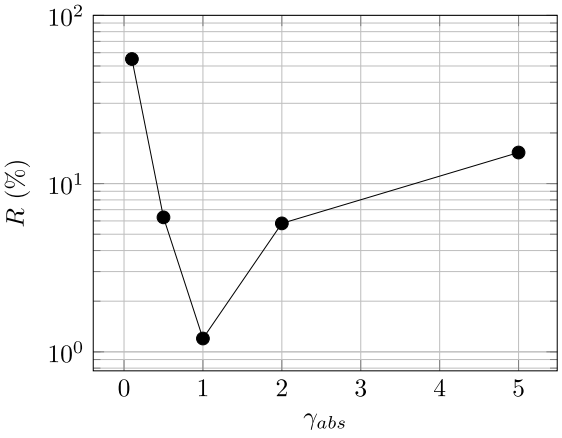

Fig. 9. Influence of the damping intensity on the reflection coefficient measured upstream of the damping region for waves with $T = 15\,\mathrm{s}$, $H = 5.75\,\mathrm{m}$, and a depth of $h = 27\,\mathrm{m}$.

and a depth of $h = 27\,\mathrm{m}$. As already stated $L_{abs} = \lambda$. Wave gauges are respectively located at $x_1 = 3\lambda$ and $x_2 = 3.25\lambda$. The selected spatial and temporal discretization parameters are known to be suited to the simulation of wave propagation in *seine3d* alone and will serve as a basis for the coupled simulations to come. *seine3d* boundary elements are given longitudinal and vertical dimensions of $\Delta x = \lambda/16$ and $\Delta z = h/4$, and the time step is set to $\Delta t = T/100$. The CFL is therefore estimated as:

$$\mathrm{CFL} = \sqrt{gh}\frac{\Delta t}{\Delta x} = 0.172 \tag{49}$$

The duration of the simulation is set to $50T$.

Fig. 8 shows the SF and simulated free surface position time histories in the most advantageous case with $\gamma_{abs} = 1$ and $R = 1.2\%$. Such a reflection rate is satisfactory and even though lower values may be attainable, they are not sought in this work. It should be noted that the simulation takes approximately $20T$ to stabilize, with the occurrence of a few overshoots. Hence making such simulations last for $50T$ seems a reasonable choice, allowing to use $20T$ or $30T$ for the spectral analysis of the signals.

The reflection rate R is also assessed for a few other values of γ_{abs}, as shown in Fig. 9. It can be seen that the influence of the damping intensity on wave absorption in *seine3d* conforms with what is intuitively expected, with a minimum for a given value of γ_{abs}. As γ_{abs} increases, the damping region behaves more and more like a solid vertical wall. Thus if γ_{abs} is too high, strong wave reflection occurs, limited to the upstream part of the damping region. Conversely, as γ_{abs} decreases, the absorbing layer tends to full transparency, and the waves can go through it without being sufficiently attenuated and reflection then occurs on the downstream boundary of the numerical domain.

This damping behavior still holds in the case of the other design waves considered in this study. Indeed, the same value of $\gamma_{abs} = 1$ also yields very low reflection rates for waves with $T = 12\,\mathrm{s}$ and $T = 9\,\mathrm{s}$.

5.2.2. Velocity field in *seine3d* simulations

It has been established that the simulated and SF free surface time profiles match quite well, even with arbitrarily chosen *seine3d* numerical parameters: $\Delta x = \lambda/16$, $N_z = 6$ and $\Delta t = T/100$. We now make sure that the velocity field obtained by *seine3d* comply with the SF ones built from the SF algorithm. It is of central interest, as the coupling methodology relies on the exchange of vertical profiles of velocity between *seine3d* and *CS*. Such a comparison is displayed in Fig. 10 at 5 time instants between $t = 49T$ and $t = 50T$.

Overall, velocity profiles match quite well, and it is difficult to distinguish solutions corresponding to the various combinations of parameters tested. Small but notable discrepancies take place between $t = 49.6T$ and $t = 49.8T$ for the horizontal velocity and at $t = 49T$ for the vertical velocity, at the very end of the simulation time.

We might therefore conclude that the spatial and temporal discretizations employed as default values in *seine3d* calculations, namely $\Delta x = \lambda/16$, $N_z = 4$ and $\Delta t = T/100$ (leading to a CFL of 0.172) are adapted for further use in coupled simulations with $\epsilon = 1/40$ and $T = 15\,\mathrm{s}$. These spatial and temporal discretization levels thus serve as a basis to model the propagation of regular waves in coupled potential domains, but are adapted to suit constraints inherent to the coupling with *CS* instances.

5.3. Parameter choice in *CS*

Similarly to what has been done with simulations involving only *seine3d*, a correct combination of time step and computational cell size is sought for *CS*, for a wave steepness $\epsilon = 1/40$.

5.3.1. Simulation setup for tests in *CS*

A numerical domain length of 4 wavelengths is used. One wavelength is dedicated to wave generation at one end of the domain, whereas a wave-damping region of the same length occupies the other end. The vertical walls and the domain bottom are set to a free-slip condition for the velocity, consistent with the fact the wall boundary layers are neglected. Homogeneous Neumann conditions are imposed on the air fraction and pressure. An *Imposed Pressure Outlet* boundary condition consisting of a Dirichlet boundary condition on pressure alongside with homogeneous Neumann conditions on the velocity components and the air fraction is set at the top of the domain. A detailed

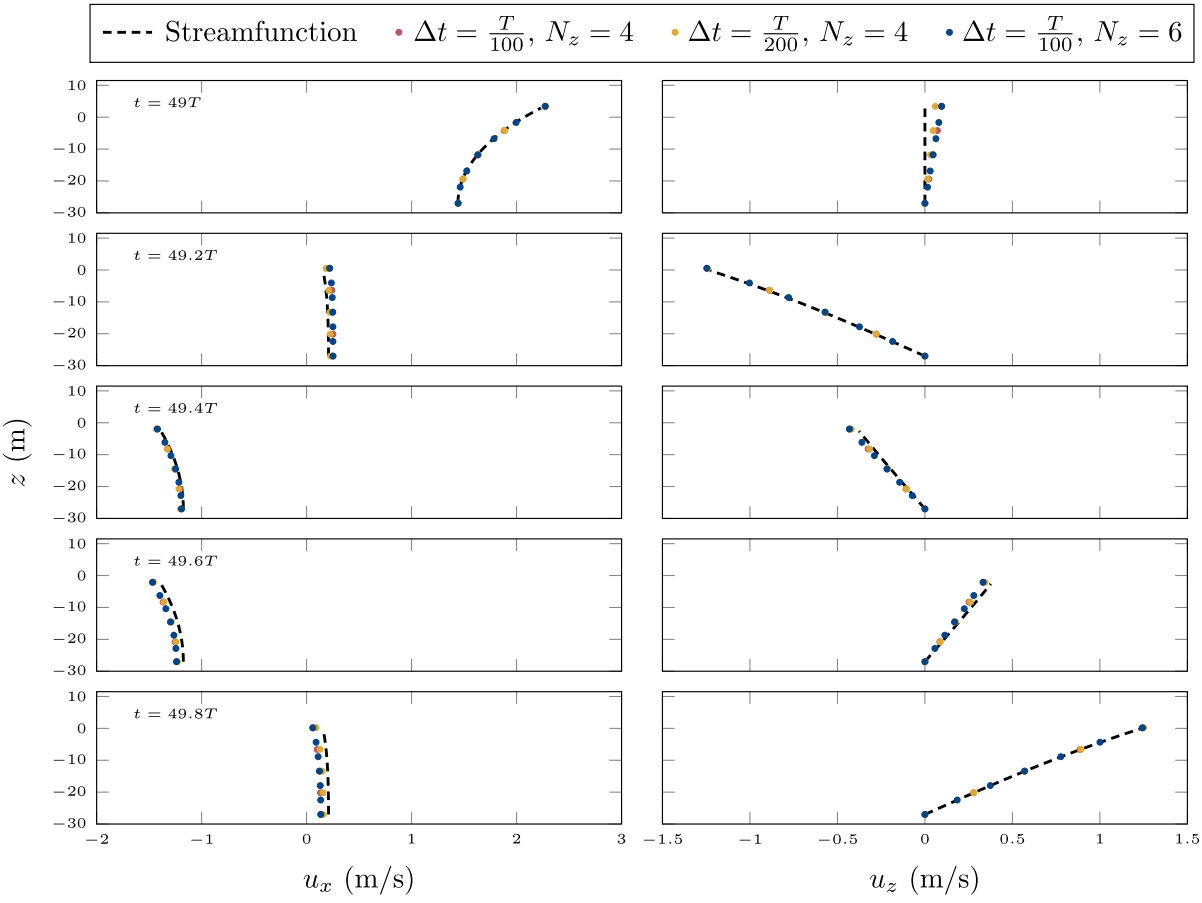

Fig. 10. Vertical profiles of *seine3d* horizontal (left) and vertical (right) velocity at the virtual abscissa of the monopile ($x = 0.0$ m) during the 50th wave period for several values of Δt and N_z. Δx is set to $\lambda/16$.

description of the different types of boundary conditions in *CS* may be found in the theory guide (Code Saturne development team, 2019).

To reduce the number of cells in the associated computational mesh, the vertical dimension of the cells is not uniformly distributed. Indeed, and as a default choice, Δz is set to $H/20$ around the free surface, and it gradually increases up to $H/4$ near the floor and ceiling of the *CS* domain. With the same goal in mind, a longitudinal cell aspect ratio of 4 is chosen in the vicinity of the free surface, with $\Delta x = H/5$. A first value for the *CS* time step size was selected based on two previous results, namely the fact that $\Delta t_{seine3d} = T/100$ was found to be a correct value for *seine3d* regular wave simulations, and that time steps ratios in the order of 10 or 15 proved relevant in the coupled simulation of solitary wave propagation (not shown here, see Landesman, 2022). Thus the step size verifies $\Delta t = T/1500$. The CFL value becomes:

$$CFL = \sqrt{gh}\frac{\Delta t}{\Delta x} = 0.14 \tag{50}$$

Note that some of these choices are challenged in Section 5.3.4. It was also decided to keep using conforming hexahedral meshes in simulations involving *CS* only, at the cost of using rather high cell aspect ratios. Indeed, it should be recalled that only conforming grids are dealt with in the coupling strategy, or at least meshes with conforming parts in the overlapping regions associated with the coupling instances.

Wave generation is ensured by a Dirichlet condition on velocity and air fraction at the upstream (inlet) boundary face associated with an additional source term in the air fraction transport equation. The vertical position reached by the free surface at the inlet face, as well as the vertical profiles of both velocity components u_x and u_z, needed to set the Dirichlet condition, are provided by a program implementing the semi-analytical SF wave algorithm of Fenton (1999). A negative homogeneous horizontal current is added to u_x to ensure that Stokes drift is canceled. To absorb waves, similar source terms affecting a damping region located at the other end of the tank are added to the same equations.

Here a brief overview of these source terms is given. Generalizing Eq. (10) and (11) with modified pressure to the case where a non-zero mass source term S and a user-defined momentum source term $S_{\mathbf{u}}$ exist, one gets:

$$\frac{\partial \rho}{\partial t} + \nabla \cdot (\rho \mathbf{u}) = S \tag{51}$$

$$\frac{\partial \rho \mathbf{u}}{\partial t} + \nabla \cdot (\rho \mathbf{u} \otimes \mathbf{u}) = -\nabla p + \nabla \cdot \mathbb{T} + (\rho - \rho_{air})\mathbf{g} + S_{\mathbf{u}} \tag{52}$$

Making use of the conservation equation to develop the instationary term $\frac{\partial \rho \mathbf{u}}{\partial t}$ in the momentum equation, one obtains:

$$\rho \frac{\partial \mathbf{u}}{\partial t} + \nabla \cdot (\rho \mathbf{u} \otimes \mathbf{u}) - \mathbf{u}\nabla \cdot (\rho \mathbf{u}) = -\nabla p + \nabla \cdot \mathbb{T} + (\rho - \rho_{air})\mathbf{g} + S_{\mathbf{u}} - \mathbf{u}S \tag{53}$$

The VOF system of equations under the incompressible flow assumption can then be recalled:

$$\frac{\partial \rho \mathbf{u}}{\partial t} + \nabla \cdot (\rho \mathbf{u} \otimes \mathbf{u}) = -\nabla p + \nabla \cdot \mathbb{T} + (\rho - \rho_{air})\mathbf{g} \tag{54}$$

$$\nabla \cdot \mathbf{u} = 0 \tag{55}$$

$$\frac{\partial \alpha}{\partial t} + \nabla \cdot (\alpha \mathbf{u}) = 0 \tag{56}$$

Mass conservation in the VOF model is therefore:

$$\left[\frac{\partial \alpha}{\partial t} + \nabla \cdot (\alpha \mathbf{u})\right] + \frac{\rho_{water}}{\rho_{air} - \rho_{water}} \nabla \cdot \mathbf{u} = 0 \tag{57}$$

A forcing source term S_α can be added to the air fraction transport Eq. (56), following:

$$S_\alpha = \Gamma_\alpha^{frc}(\alpha_{ref} - \alpha) \tag{58}$$

with α_{ref} a reference air fraction field towards which the computed field is forced and Γ_α^{frc} a forcing coefficient having the dimension s^{-1}. Hence, a corresponding source term S_α^* has to account for changes in the volume conservation Eq. (55)

$$S_\alpha^* = -\frac{\rho_{air} - \rho_{water}}{\rho_{water}} \Gamma_\alpha^{frc}(\alpha_{ref} - \alpha) \tag{59}$$

so that Eq. (57) still holds.

Similarly, considering a momentum source term injected in Eq. (54) with $\mathbf{u}_{ref}$ a target velocity field, it comes:

$$S_\mathbf{u} = \Gamma_\mathbf{u}^{frc} \rho(\mathbf{u}_{ref} - \mathbf{u}). \tag{60}$$

These source terms have an implicit part, involving the relevant scalar or vector field α or $\mathbf{u}$, and an explicit one to take into account the reference solution. It should also be noted that $S_\mathbf{u}$ operates in both phases.

The VOF system of equations then becomes:

$$\frac{\partial \rho \mathbf{u}}{\partial t} + \nabla \cdot (\rho \mathbf{u} \otimes \mathbf{u}) = -\nabla p + \nabla \cdot \mathbb{T} + (\rho - \rho_{air})\mathbf{g} + S_\mathbf{u} - \mathbf{u} S_\alpha^* \tag{61}$$

$$\nabla \cdot \mathbf{u} = S_\alpha^* \tag{62}$$

$$\frac{\partial \alpha}{\partial t} + \nabla \cdot (\alpha \mathbf{u}) = S_\alpha \tag{63}$$

In the wave generation region, α_{ref} is based on the free surface profile provided by the SF wave algorithm, i.e., it is set to 0 if the vertical coordinate of the considered computational cell's center is lower than the SF value, and to 1 otherwise. Accordingly, $\mathbf{u}_{ref}$ is built using the SF velocity field. In the damping region, the same strategy is implemented for α_{ref} based on the resting free surface level, while $\mathbf{u}_{ref}$ is simply set to zero.

The forcing coefficients Γ_f^{frc}, where f stands for α or $\mathbf{u}$, are modulated by a spatially varying blending function $\omega(\mathbf{x})$.

$$\Gamma_f^{frc} = \omega(\mathbf{x})\, \gamma_f^{frc} \tag{64}$$

with γ_f^{frc} the forcing intensity.

As described in , the selected blending function takes the value 1 at the inlet boundary and exponentially decreases down to 0 at the end of the generation region. The opposite is true for the absorbing layer. For wave generation, a suitable value of γ_{frc} is found following a trial-and-error approach in which the simulated free surface profiles at the beginning of the simulation – as long as waves have not started to interact with the downstream damping layer – are compared to their SF counterparts. To absorb waves, the forcing intensity is selected after a series of tests in which, as in , the smallest possible reflection rate R is sought.

By successive improvements, a working setup was found for the wave case investigated in this section. In the damping layer, γ_α^{frc} is identical to $\gamma_\mathbf{u}^{frc}$ while $\gamma_\mathbf{u}^{frc}$ equals zero in the generation area. Values of γ_α^{frc} differ by nearly two orders of magnitude in both regions. Optimal values were found to depend on the wave conditions. As we do not make use of wave generation and absorption capabilities of *CS* in the coupled simulations, a more exhaustive study of the related parameter influence is therefore not shown here.

5.3.2. Analysis of free surface elevation signals

In general, the free surface elevation produced by *CS* is satisfactory. It should also be noted that all the results displayed in this section were obtained using a design wave with $T = 15\,s$ and $H = 5.75\,m$; see also Table 1. Consider the free surface spatial profiles in the whole *CS* domain at two different time instants ($t = 5T$ and $50T$) in Fig. 11.

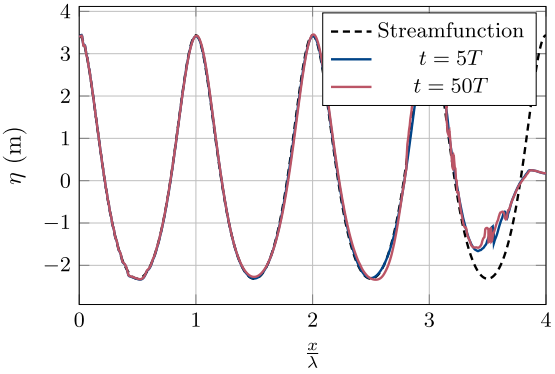

Fig. 11. Comparison of the SF and computed free surface profiles at time instants $t = 5T$ and $t = 50T$ in a test simulation involving only *CS*.

$t = 5T$ is deemed a sufficient initialization delay, after which waves are assumed to have fully developed in the domain. One also notes the important free surface smearing occurring in the absorbing region, due to the forcing brought by the additional source terms. Free surface smearing gradually extends upstream as the computation advances, as can be noticed by comparing both colored curves. Away from the damping zone and its close vicinity, the simulated free surface profiles agree well with the SF one. Hence, to avoid disturbances in the free surface profile it seems reasonable not to consider results farther than $x = 2.5\lambda$.

5.3.3. Assessment of wave kinematics

The free surface shape remaining satisfactory on most of the domain through time, we should now assess the quality of the simulated kinematics beneath the wave, as this is necessary for the accuracy of force calculations in wave–structure interactions. To that end, the fields of u_x and u_z in the water phase are shown at time instants $t = 5T$ in Fig. 12a. The corresponding SF free surface position is also pictured as a reference, and we may once again notice that the simulated free surface solution looks well for $x < 2.5\lambda$ at least.

The velocities appear more problematic, with spurious velocity patterns appearing close to the free surface slightly upstream of $x = 2.5\lambda$ at $t = 50T$. Their horizontal extent seems correlated to that of the chaotic free surface area, that expands from 3λ to 4λ. Away from this region, however, the velocity components seem to agree with what is expected, except close to the wave generation boundary. Therefore, a quite conservative choice is made to restrict the working length of the *CS* domain to the area enclosed between $x = \lambda$ and $x = 2.25\lambda$, for the whole duration of the simulation. $x = 2\lambda$ is thus chosen to extract and compare the vertical profiles of velocity.

Fig. 13a depicts the vertical profiles of horizontal velocity at different time instants when the theoretical wave crest passes $x = 2\lambda$. A continuous worsening of the horizontal velocity profile is observed through time, as the velocity is overestimated close to the free surface and underestimated near the bottom. A study of the phase error in wave propagation showed errors under 2°, and cannot explain these discrepancies alone.

These results are somewhat similar to those obtained by Larsen et al. (2019) and references therein with Interfoam, considering the propagation of a SF wave under periodic boundary conditions. The increase in time of the vertical gradient of the horizontal velocity observed here is similar to what these authors noticed. In Larsen et al. (2019), it is assumed that the existence of nonphysical water velocities close to the free surface is caused by an imbalance in the momentum equation in nearby cells, originating from discretization errors in the force terms of NS equations. Due to the high-density ratio between water and air, any spurious transfer of momentum from the dense phase to the light one then leads to a large overestimation of the

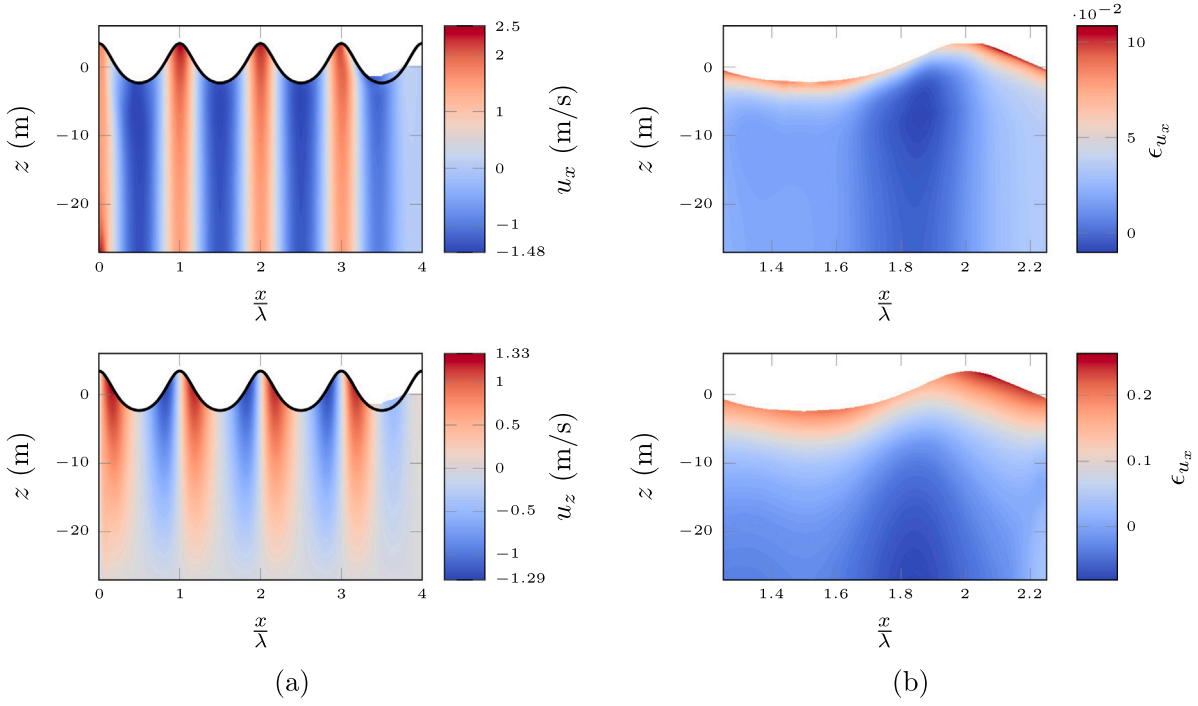

Fig. 12. Velocity field in *CS*: (a) horizontal and vertical velocity components at $t = 5T$ with SF free surface profile in black; (b) normalized error on the horizontal velocity over one wavelength, at time instants $t = 5T$ (top) and $t = 50T$ (bottom).

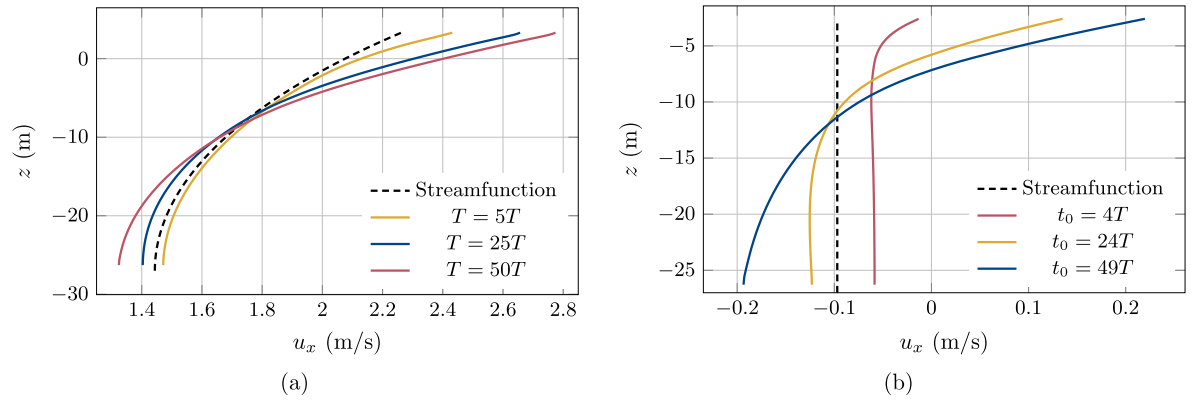

Fig. 13. Vertical profiles of the horizontal velocity beneath the wave crest at $x = 2\lambda$: (a) instantaneous values; (b) time average of the horizontal velocity over one wave period between t_0 and $t_0 + T$. The mean Eulerian horizontal velocity, as computed by the SF wave algorithm, is shown for comparison.

air velocity near the free surface. Unrealistic air velocities are then inevitably diffused back to the superficial part of the water phase, as the VOF advection scheme cannot maintain arbitrary high shearing values at the interface between the phases. As Interfoam is comparable to *CS* in its conception, these conclusions should also apply to the current study.

It appears that the velocity overestimation close to the free surface not only occurs near the wave crest. It is stronger on the quarter of the wavelength extending in front of the wave trough. Large values of ϵ_{u_x} concentrate in a layer located just beneath the interface whose thickness increases with time. Velocity underestimation close to the bottom, although smaller, grows by an order of magnitude throughout the simulation.

As a last illustration of the distortion of the vertical profiles of horizontal velocity, the time average of u_x along a vertical line located at $x = 2\lambda$ is computed. The latter extends from the bottom up to slightly under the wave trough. This maximal ordinate is taken as $z = -H/2$. Results are displayed in Fig. 13b. The computed mean profiles indicate that a clockwise circulation builds up in the bulk of the domain. A vertical gradient of mean horizontal velocity appears and grows in time, as opposed to what the SF theory predicts. The mean vertical velocity is negligible as compared to the horizontal mean and is not shown here.

For possible causes, the potential influence of the damping region on the generation of this spurious circulation should be addressed. Although the findings of Larsen et al. (2019) with Interfoam involve a periodic domain in which no absorbing layer is implemented, we cannot exclude the possibility that the velocity forcing at the downstream end of the *CS* domain has something to do with the worsening of the vertical profile of u_x, observed at least one wavelength upstream from the beginning of the damping region.

Hence, three possible explanations have been considered to describe the occurrence of the overestimation of the velocity just beneath the air/water interface: imbalance in the momentum conservation equations close to the free surface, as described by Larsen et al. (2019), inappropriate velocity boundary condition at the top in the air phase, and upstream influence of the damping region. It should be recalled that this goes along with satisfactory free surface profiles in the major part of the domain.

5.3.4. Influence of numerical parameters on the velocity

Issues concerning the agreement of the vertical profile of horizontal velocity with the reference solution have been raised in the previous section. A direct way of improving *CS* velocity results is to increase the spatial and temporal resolution of the simulations. The wave period and steepness and the domain setup are kept the same. Without exhaustiveness in mind, 3 different values of the cell aspect ratio (AR) close to the free surface at rest were tested ($AR \in \{1, 2, 4\}$) while AR = 4 is the default value previously used. The definition given for the aspect ratio is $AR = \Delta x/\Delta z$. Similarly, the performances of 3 time step sizes are assessed, namely $\Delta t = T/750$, $T/1500$, and $T/3000$, with $T/1500$ being the default setting. The cell height close to the free surface has been set to $\Delta z = H/20$, but the *CS* mesh is vertically stretched away from the free surface resting position. Simulations were run with additional values of $\Delta z = H/10$, $H/15$, and $H/50$. To save computational time, the results, shown in Fig. 14, are compared with the reference at time $t = 5T$. As the velocity overestimation was already observed at this time instant in previous simulations, it was deemed suitable and it allowed for quick computations.

The analysis of simulation outcomes is quite straightforward: of the 3 parameters of interest, the only one for which noticeable improvements are achieved as compared to the results with the default value is the time-step size. Increasing the time resolution from $T/1500$ to $T/3000$ leads to a decrease in the overprediction of horizontal velocity close to the free surface. Conversely, the vertical profiles of u_x worsen when a value of $\Delta t = T/750$ is used. At the same time, the influence of the cell AR, at least in the range considered here, is negligible. Small spurious variations close to the free surface are observed in the velocity profiles obtained using cells with a height lower than $H/20$. Increasing the vertical resolution in the free surface region up to $\Delta z = H/50$ did not improve the results.

As a result, $AR = 4$, $\Delta t = T/3000$ and $\Delta z = H/20$ thus form a set of basis parameters that are used in *CS* in coupled simulations with a wave steepness of 1/40. This yields a CFL of 0.07, as defined in Eq. (49).

To get a last insight on the quality of the wave kinematics computed using only *CS*, the vertical profiles of velocity over a whole wave period are shown in Fig. 15 at 5 stages of the simulation. Vertical profiles of u_x exhibit behaviors coherent with what has been previously observed for the horizontal velocity under the crest. Not long after the beginning of the simulation, between $t = 4T$ and $t = 5T$, u_x remains close to the SF solution for the first half of the wave period. During the other half, an almost constant offset affects the horizontal velocity, which disappears later in the simulation. u_x overestimations increase in time, mostly during the first half of the simulation, up to $t = 50T$. In general, it is hard to distinguish between curves with $t_0 = 49T$ and later $t_0 = 99T$. This indicates that the gap between the computed velocity and the reference does not continuously and monotonically drift with time, but rather seems to reach a steady value. Noticeably, agreement with the reference profile is better beneath the crest than the trough of the wave.

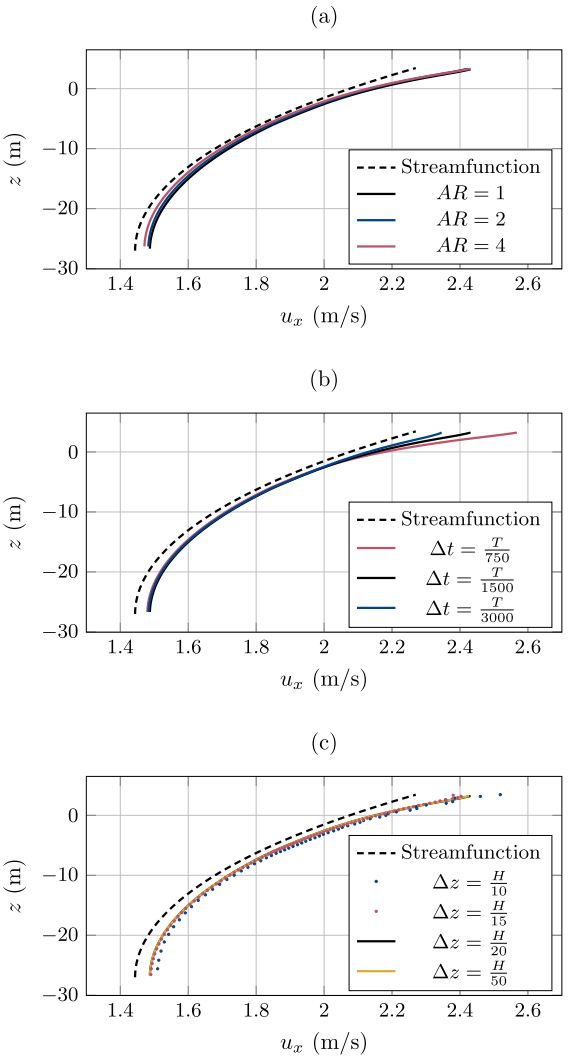

Fig. 14. Comparison of SF and computed vertical profiles of the horizontal velocity at $t = 5T$. Simulations using only *CS* with the same setup as before. (a) simulation with varying cell aspect ratio (AR), other parameters are set to $\Delta z = H/20$ and $\Delta t = T/1500$. (b) simulation with varying time-step, other parameters are set to $AR = 1$ and $\Delta z = H/20$. (c) simulation with varying cell height, other parameters are set to $AR = 1$, $\Delta t = T/1500$.

5.4. Coupled simulations in 2D

Now that suitable numerical settings have been established to simulate the generation, propagation, and absorption of regular waves with $T = 15$ s and $\epsilon = 1/40$ in both models separately, we return to the setup presented in Fig. 7 and run coupled simulations.

5.4.1. Coupling parameters

As already mentioned, specific numerical strategies and discretization levels used in *seine3d* and *CS* instances, which have been set in previous computations involving only one model, are left unchanged as much as possible. For this 2DV wave case, the only coupling parameter that is yet to be set is the length of the two overlapping regions *seine3d* 1/*CS* and *CS*/*seine3d* 2. The time step ratio $N_{\Delta t}$ is fully constrained by the choices made in model instances *seine3d* 1 and *CS*. Besides, the time step size employed in *seine3d* 1 is enforced in *seine3d* 2. Thus, from the previous section,

$$N_{\Delta t} = \frac{\Delta t_{seine3d}}{\Delta t_{\mathrm{CS}}} = 30 \tag{65}$$

as $\Delta t_{seine3d}$ was set to $T/100$ and $\Delta t_{\mathrm{CS}} = T/3000$.

$L_{overlap}$ is the same in both overlapping regions, and it is chosen arbitrarily. This takes into account the fact that at least 4 *seine3d* boundary elements in the length of the overlapping regions seem necessary, as turned out from previous solitary wave propagation simulations (Landesman, 2022). As $\Delta x_{seine3d}$ was set to $\lambda/16$ beforehand, $L_{overlap}$ is thus set to $\lambda/4$.

Based on preliminary estimations and general guidelines concerning both models' behavior, 19 and 15 CPU cores are attributed to *seine3d* 1 and *seine3d* 2 respectively, while *CS* uses 2 cores. This way the computation requests one 36-cores node from the computing cluster. Such breakdown of computing power is somewhat not intuitive, as *seine3d* is supposed to be less computationally expensive than *CS*, but here requires more cores per wavelength. As its name suggests though, *seine3d* is a 3D code and 4 boundary elements fit the potential domain's

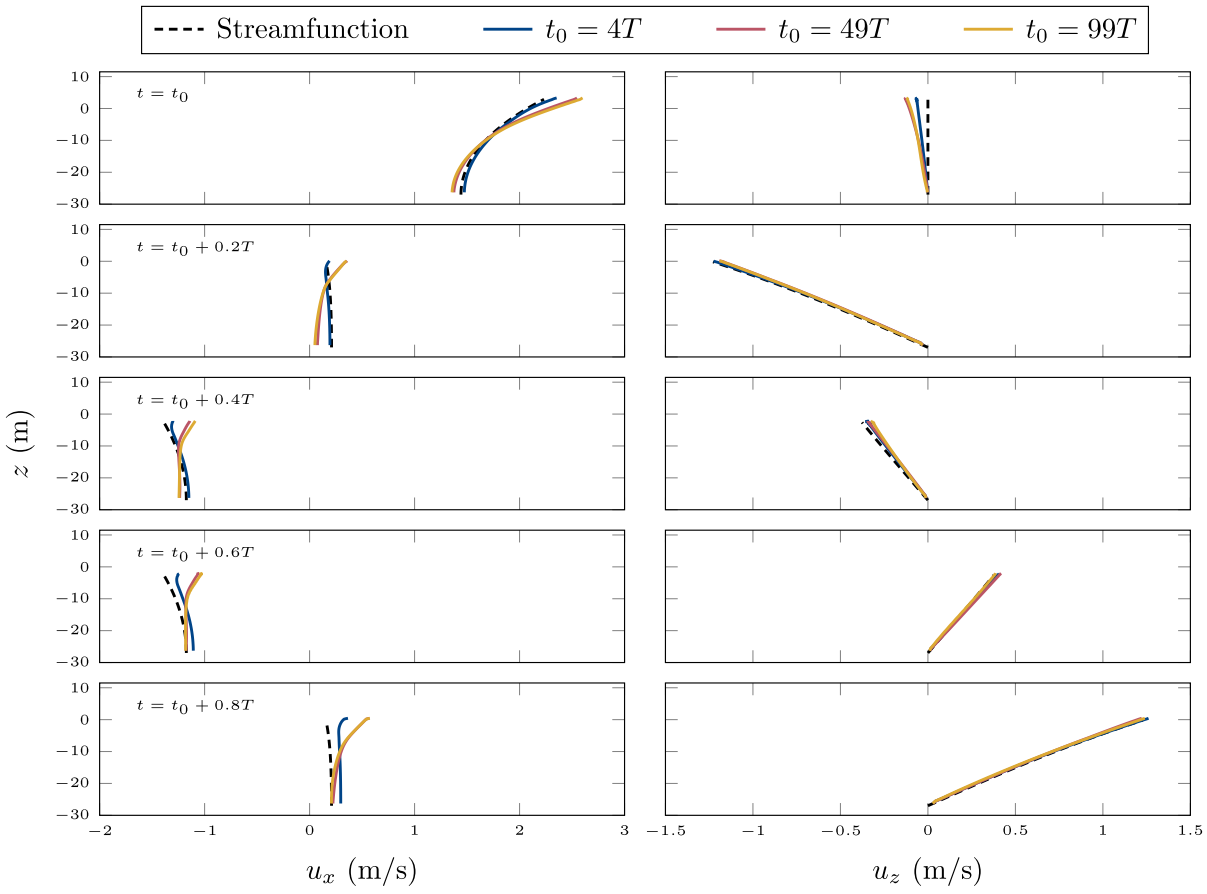

Fig. 15. Vertical profiles of horizontal (left) and vertical (right) velocity at $x = 2\lambda$ during one wave period just before $t = 5T$, $t = 50T$ and $t = 100T$. Simulation using *CS* only.

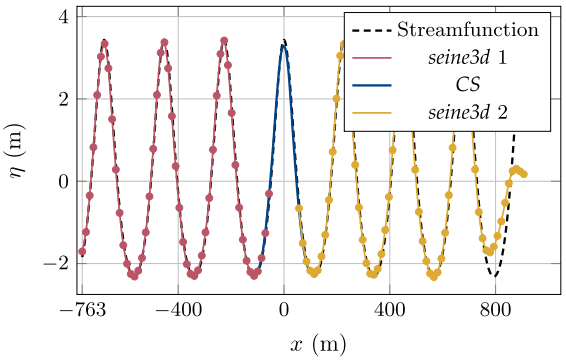

Fig. 16. Instantaneous free surface profiles from coupled model instances at $t = 50T$. Circles mark the position of *seine3d* free surface nodes.

width. On the opposite, there is only one cell in the width of *CS* domain. Therefore computational efficiency is of no interest here, but is addressed while discussing 3D simulations below. We might however indicate that it takes about 10 h to reach a physical time equivalent to $50T$.

5.4.2. Simulation results

Fig. 16 shows the global free surface profile after 50 wave periods. The agreement with the SF reference solution is satisfactory. In particular, free surface matching is ensured in the two overlapping regions. It is interesting to note that, at this time instant at least, the wave height is slightly lower in *CS* than in the neighboring potential domains. A close study of the profiles indicates that almost no wave reflection is experienced from the presence of overlapping regions.

To further assess the relevance of the coupling methodology applied to regular wave simulations, the velocity fields are compared around $t = 50T$ in both overlapping regions in Fig. 17. A good overall agreement is seen. Discrepancies are observed close to the free surface, the largest ones on the upstream boundary of the *seine3d* 2 domain. They should be linked to edge/corner singularities in *seine3d*. Other discrepancies seem to originate from the viscous domain, as *CS* velocities quite systematically slightly exceed the *seine3d* velocity close to the free surface.

As a final comparison of the kinematics, the vertical profiles of velocity extracted from the central *CS* domain are juxtaposed to the ones predicted by the SF solution (Fig. 18). To allow enough time for the waves to build, the wave period considered is the 20th. The results resemble those depicted in Fig. 15, thus they are not further described. The coupling procedure clearly reproduces the behaviors experienced in each model alone.

5.4.3. Coupled model limitations for wave steepness

To consider a more nonlinear case, regular waves with a steepness of 1/22 are simulated, again with the domain shown in Fig. 7. Such value of ϵ corresponds to the highest non-linear wave considered in the study of Dadmarzi et al. (2019) for which results of force on the monopile are reported. To reach it, a target wave height of $H = 10.5\,\mathrm{m}$ is associated with a wavelength of $\lambda = 231.7\,\mathrm{m}$ using the SF algorithm of Dean (1965) implemented in *seine3d*.

Normalized spatial and temporal resolution levels used in the case of the mildly nonlinear wave with $\epsilon = 1/40$ are retained in the first attempt. In *seine3d* instances, the boundary element dimensions at rest are $\Delta x_{seine3d} = \lambda/16$ and $\Delta z_{seine3d} = h/4$, with $\Delta y_{seine3d} = \Delta x_{seine3d}$. The *CS* mesh is built with the same rules in mind as before, namely $\Delta z_{CS} = H/20$ close to the free surface, progressively stretched to $H/4$ near the

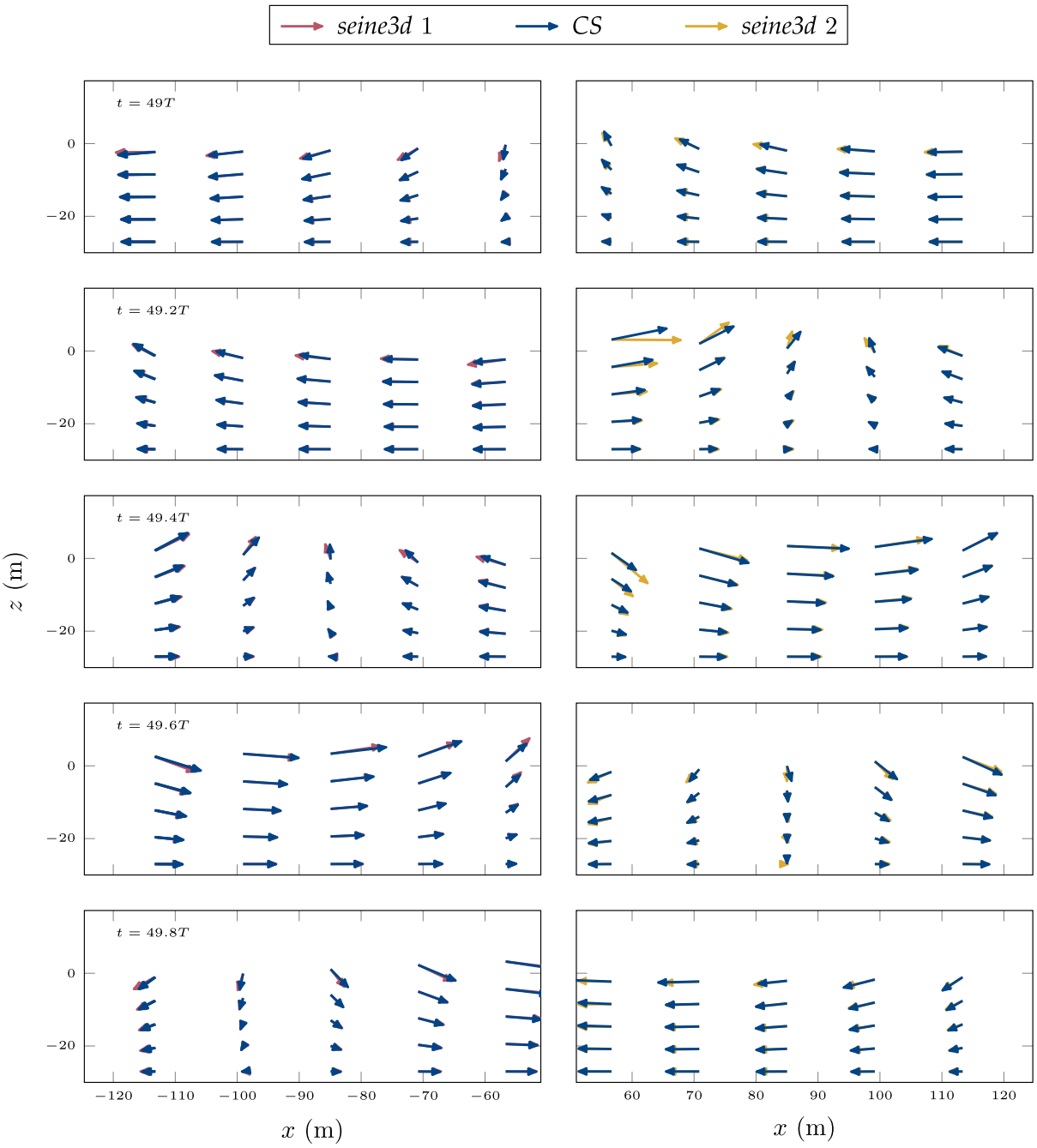

Fig. 17. *CS* and *seine3d* velocity fields in $\Omega_{overlap}$ and for each coupling during the 50th simulated wave period. Velocity is extracted at the location of *seine3d* boundary nodes.

floor and ceiling. $\Delta x_{CS} = H/5$: this corresponds to a longitudinal aspect ratio of 4 near the interface. The time step sizes are set to $T/30$ and $T/1500$ for *seine3d* and *CS* respectively, yielding a time step ratio of 15. The theoretical CFL in potential domains can be established as:

$$CFL_{seine3d} = \sqrt{gh}\frac{\Delta t_{seine3d}}{\Delta x_{seine3d}} = 0.169 \tag{66}$$

In *CS*, it is approximated as:

$$CFL_{CS} = \sqrt{gh}\frac{\Delta t_{CS}}{\Delta x_{CS}} = 0.562. \tag{67}$$

Therefore, the time-step ratio is $N_{\Delta t} = 50$. With this, the simulation ran well, with slightly higher errors in the results as compared to the theory.

Note that a preliminary test with a smaller time-step for *seine3d* became unstable after $20T$. However, it was reported in a recent work involving *seine3d* in its current state (Harris et al., 2022), using the same boundary surface description method and time-stepping procedure, that generation and propagation of SF waves were ensured in *seine3d* up to a steepness of $\epsilon = 0.092$. As it is equivalent to more than twice the wave steepness used here, it implies that the case of $\epsilon = 1/22$ should not raise issues in *seine3d*, but may be an issue with the coupling for steep waves.

6. Diffraction by a vertical cylinder

6.1. Numerical setup

In this section, 3D coupled simulations of nonlinear regular waves interacting with a surface-piercing vertical cylinder representing a large offshore wind turbine foundation are presented, matching the WAS-XL measurement campaign (Dadmarzi et al., 2019). The mesh is essentially

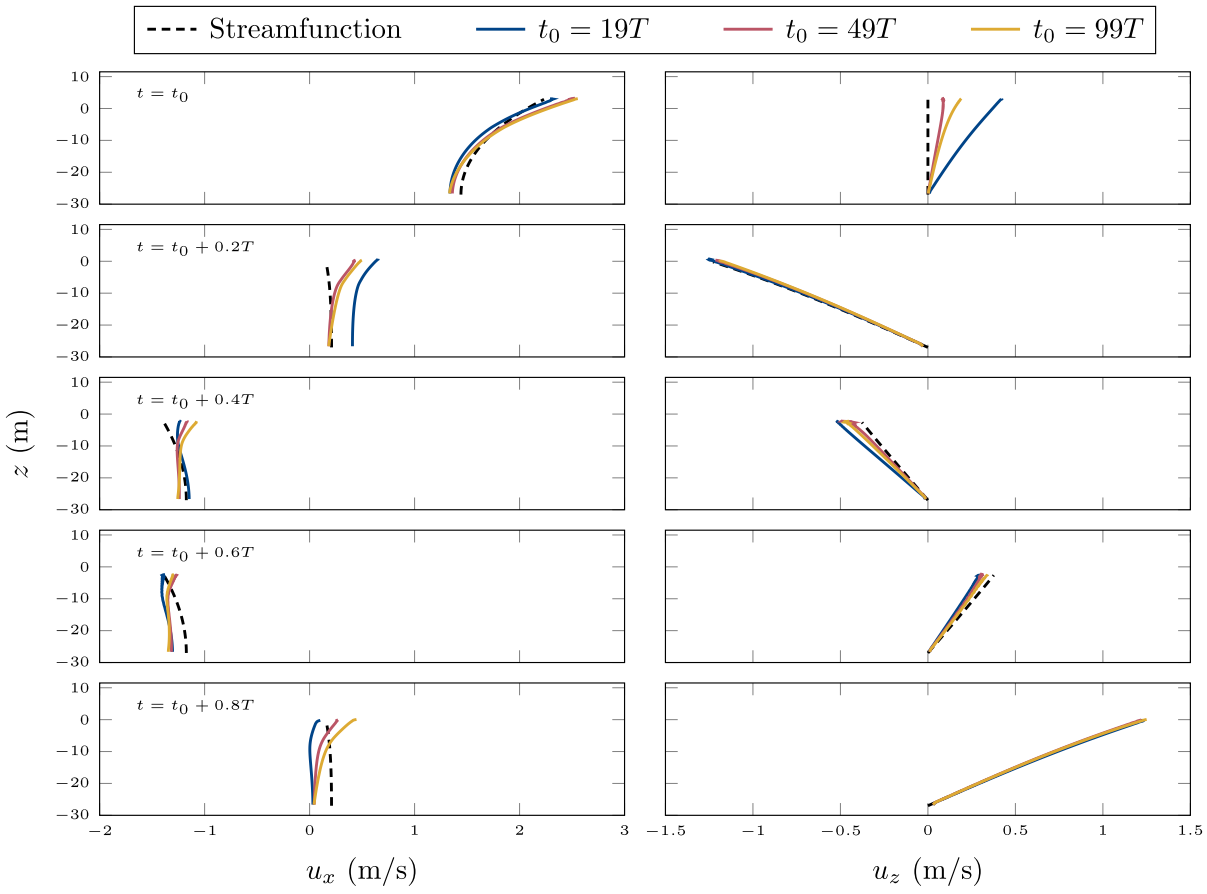

Fig. 18. Vertical profiles of *CS* horizontal (left) and vertical (right) velocity in a coupled simulation, compared to the reference SF solution, just before $t = 20T$, $t = 50T$ and $t = 100T$.

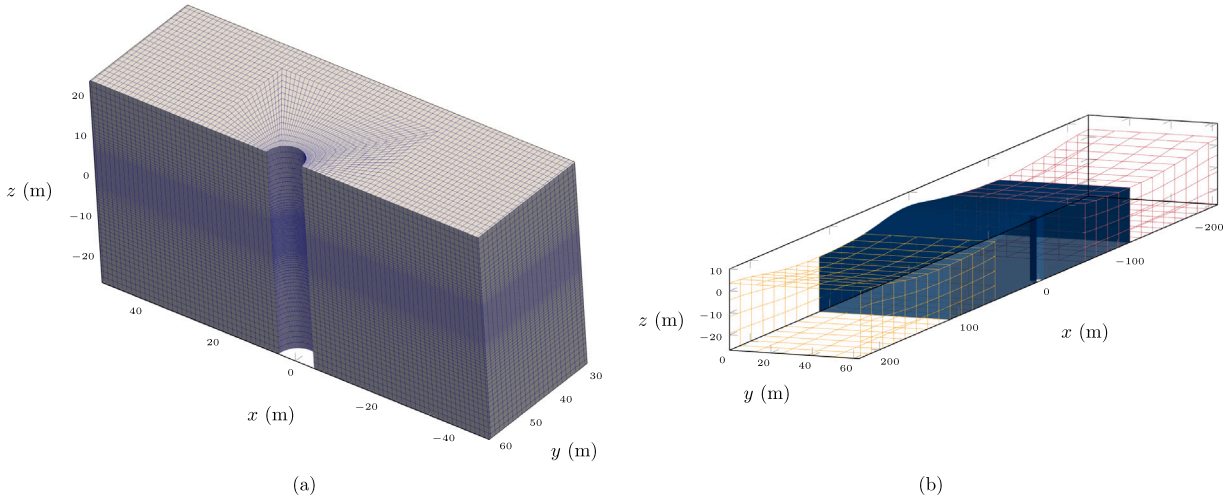

Fig. 19. Computational domains for the 3D case with $T = 15$ s and $\epsilon = 1/40$: (a) close-up view of the *CS* mesh in the vicinity of the monopile; (b) view of the coupled computational domains.

identical to the 2DV domain, extruded horizontally (in the y direction), except for the structure. The intrinsic symmetry of the problem is taken into account to halve the numerical domain size. A free-slip (symmetry) boundary condition is enforced on the cylinder surface, as well as on all vertical walls and bottom, where the velocity vector satisfies $\partial \mathbf{u}/\partial n = 0$.

In the experimental study of Dadmarzi et al. (2019), two water depths are considered in the basin, namely 27 m and 33 m at prototype scale, in which two monopile models are placed whose respective diameters are 9 m and 11 m. Here, only the case with 27 m depth and $D = 9$ m diameter is considered. Similar to the above, the wave steepness is defined as the first-order wave height divided by the wavelength. Four different wave conditions are reproduced from the WAS-XL campaign, with two values of the wave steepness H/λ: 1/40 and 1/22. For the lower wave steepness, the wave conditions are summarized in Table 1. Three wave periods are considered with $h = 27$ m and $D = 9$ m: 9 s, 12 s, and 15 s, the latter corresponding to the

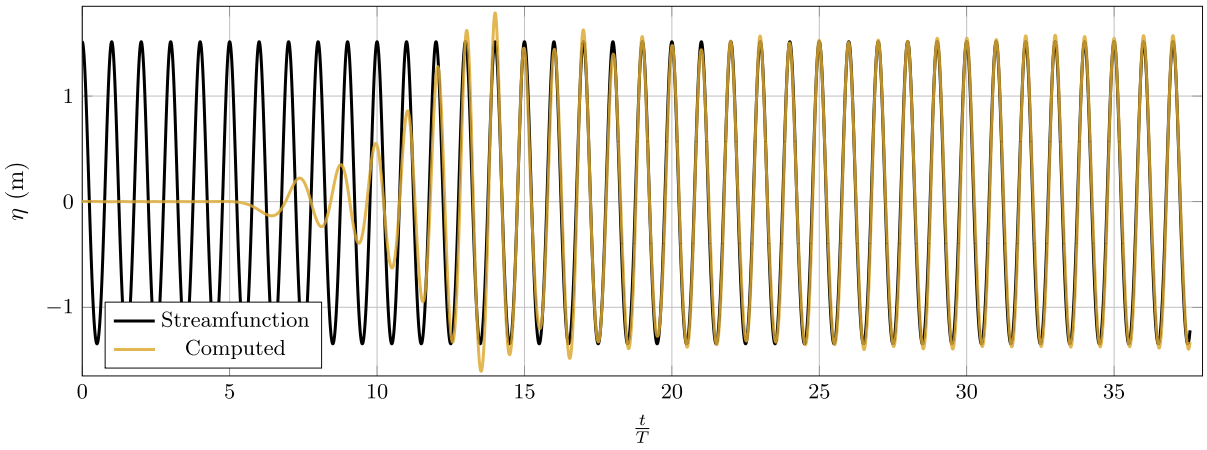

Fig. 20. Comparison of SF and computed free surface signals at the wave gauge closest to the monopile for $T = 9\,\mathrm{s}$ and $\epsilon = 1/40$.

case extensively studied in 2D in Section 5. For the more exploratory case of 1/22 steepness, only a period of 15 s is investigated, associated with a wave height of $H = 10.5\,\mathrm{m}$.

The time discretization as well as the vertical and longitudinal spatial resolutions, normalized using the wave characteristics, are kept the same in code instances *seine3d* 1 and *seine3d* 2, as well as all other parameters and options, such as solver or time-stepping scheme choices (similar to the earlier Fig. 7). Similarly, most *CS* numerical parameters are left unchanged and follow the relations established in Section 5. A computational mesh with a body-fitted description of the monopile surface is built (Fig. 19). Most meshing specifications elaborated in 2DV cases are met, i.e., Δx_{cs} and Δy_{cs} equal $H/5$ in most of the domain, away from the close vicinity of the monopile. $\Delta z_{\mathrm{cs}} = H/20$ is verified in a layer comprised between $z = -H/2$ and $z = H$. The length of the overlapping regions between *CS* and *seine3d* domains equals $\lambda/4$, as established in 2DV studies. To match the characteristics of the experimental wave basin, the width of the domain is set to 62.5 m. $\Delta x_{seine3d}$ is kept equal to $\lambda/16$, while $\Delta y_{seine3d}$ is given the value of $\Delta x_{seine3d}$ in both *seine3d* instances. A target value of $\Delta z_{seine3d} = h/4$ where the free surface is at rest is retained.

Coupled setup. For the 1/40 steepness, following the conclusions of the sensitivity analysis conducted in Section 5.3.4, Δt_{cs} is set to $T/3000$, thus setting the value of the time step ratio to $N_{\Delta t} = 30$. In accordance with the 2DV coupled wave simulations, $\Delta t_{seine3d} = T/100$.

As mentioned, for the coupled setups, slightly different domains were used for each case, to scale with the wavelength. For $T = 9\,\mathrm{s}$, the mesh in the domain *seine3d* 1 had 3219 nodes, while the one in the domain *seine3d* 2 had 1929 nodes, and the *CS* computational mesh comprised 2 400 293 cells. For $T = 12\,\mathrm{s}$, *seine3d* 1 mesh had 1701 nodes, while *seine3d* 2 mesh had 1533 nodes, and the *CS* mesh comprised 1 144 443 cells. For $T = 15\,\mathrm{s}$, *seine3d* 1 mesh had 1181 nodes, while *seine3d* 2 mesh had 1401 nodes, and the *CS* mesh comprised 652 859 cells.

For the 1/22 steepness, $\Delta t_{seine3d}$ is set to $T/30$ and Δt_{cs} takes the value $T/1500$, yielding $N_{\Delta t} = 50$. The rules governing the geometry of the different 3D subdomains are kept the same, and the wave-damping parameters are left untouched. As *CS* mesh cell dimensions are based on fixed fractions of H, the body-fitted mesh used in the current case is the smallest built for a 3D coupled simulation, with 121 783 elements. Hence, a single 36-core computing node is required to run the simulation, as 4 CPU cores are attributed to *CS*, while *seine3d* 1 and *seine3d* 2 are given 15 and 17 respectively. 100 wave periods are simulated in little more than one day with this setup.

CS -only setup. A *CS*-only computation is set up with the same numerical parameters as used in the *CS* instance for the coupled simulation with $T = 9\,\mathrm{s}$. A mesh describing the whole domain is built with 29 181 137 cells. Its part encompassing the monopile is the same as in the associated coupled simulation. Wave generation and absorption are realized with damping regions involving source terms added to the air fraction and momentum conservation equations, as described in Section 5.3. Each region is one wavelength long, thus the *CS*-only numerical domain is one wavelength longer than the global hybrid one, as wave generation is limited to the upstream boundary only in the domain *seine3d* 1, in the hybrid case. The damping intensity, whose optimal value is not independent of the wave conditions, is selected in both regions after a brief sensitivity analysis conducted on 2DV wave simulations.

6.2. Free surface elevation

The free surface time signals at the reference wave gauge are shown in Fig. 20. A duration of around $20T$ is needed from the initial stage of the computation to reach a stabilized wave regime. Free surface overshoots may be due to spurious wave reflection taking place in the damping region, implemented at the downstream end of the domain *seine3d* 2.

Close-up views of the free surface shape are displayed in Fig. 21, at 6 time instants after a wave crest has passed the monopile. A notable upstream propagating wave can be seen, as well as strong wave run-ups on the cylinder walls. Results conform rather well, qualitatively speaking, with the free surface snapshots describing the interaction of highly nonlinear non-breaking unidirectional waves with a bottom-mounted circular cylinder reported by Paulsen (2013), Paulsen et al. (2014).

6.3. Spectral analysis of horizontal force

The time history of the normalized horizontal force is partly shown in Fig. 22 after 40 wave periods. Even with a moderate wave steepness of 1/40, nonlinearities are noticeable. The agreement of coupled simulations with experimental results is assessed through the comparison of the frequency contents of the time signals recorded for the depth-integrated inline force on the cylinder. In Dadmarzi et al. (2019), the amplitudes of the first three harmonics of the normalized horizontal load on the monopile are provided for wave periods in the time range [6 s, 16.5 s], where harmonic amplitudes are extracted with a narrow-banded filter based on the Fast Fourier Transform (FFT). In the current study, a short-time Discrete Fourier Transform (DFT) is applied to the wave elevation and inline force time signals, with a one-wave period sliding window.

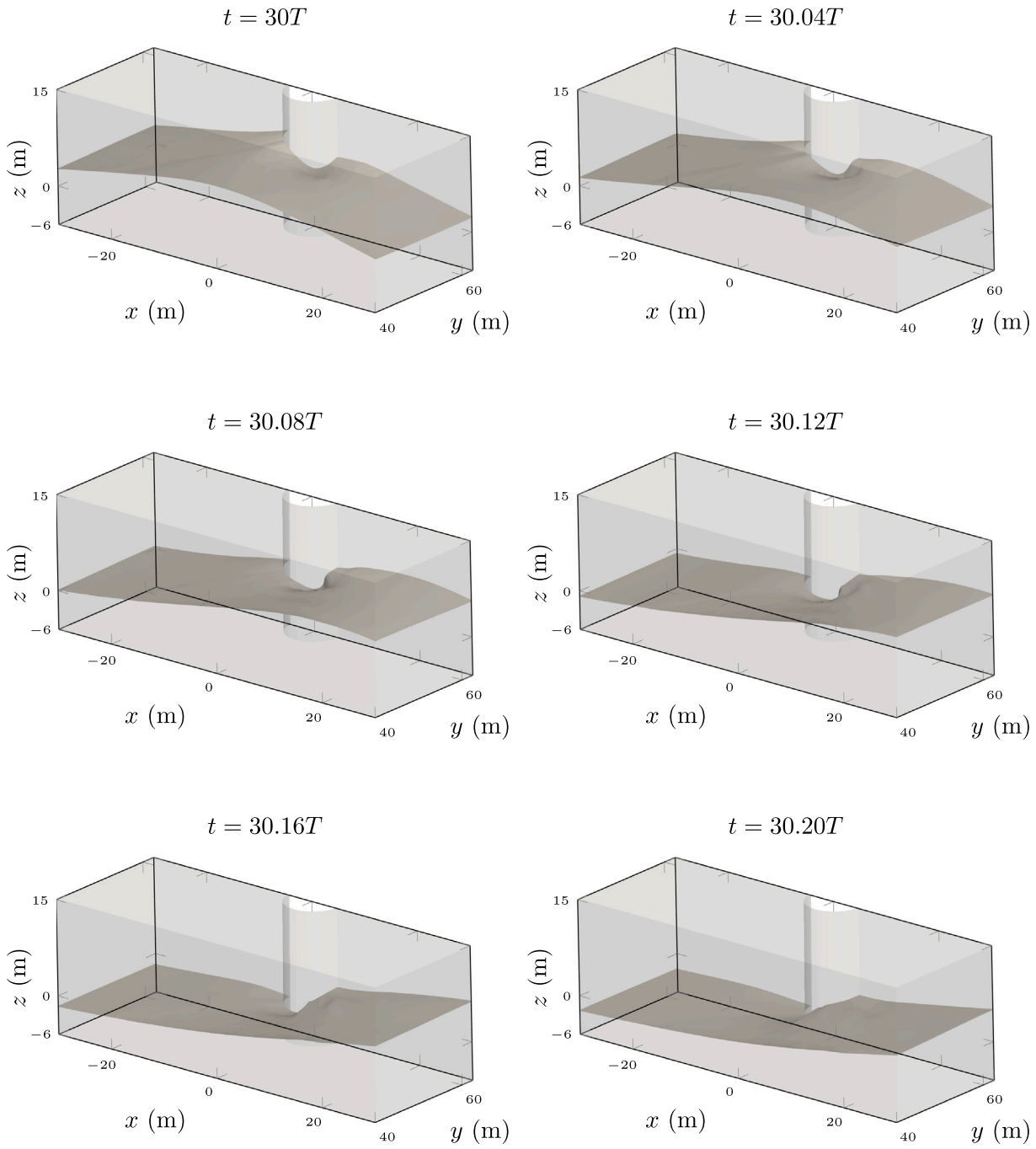

Fig. 21. Snapshots of the free surface in the *CS* domain near the monopile, as a wave crest passes, with $T = 15\,\mathrm{s}$ and $\epsilon = 1/22$. Incident waves come from the left.

The amplitude of the i^{th} harmonic of the depth-integrated inline force is normalized as follows:

$$F_x^{(i\omega)} = \frac{F_x^{(i\omega),\dim}}{\rho g a^2 A_1} \tag{68}$$

where $F_x^{(i\omega),\dim}$ is the horizontal force of the i^{th} harmonic of the wave frequency $\omega = \frac{2\pi}{T}$, a the monopile radius, and A_1 the amplitude of the first harmonic of the free surface elevation, recorded next to the monopile. From here on, ρ designates ρ_{water} for brevity in experimental comparisons.

Table 2 presents a summary of the time-averaged results. The agreement between experimental and simulated first-order results is satisfactory. Discrepancies are larger for second and third orders, but the absolute normalized amplitudes of F_x are 1 to 2 orders of magnitude lower. Hence, the implemented coupling procedure allows for simulating wave diffraction by a vertical cylinder for a moderate wave steepness, for various values of relative water depth and relative monopile radius.

6.4. Computational time

To conclude on the relevance of the BEM-VOF coupling procedure, is it necessary to have at least one comparison point available with a *CS*-only simulation. *CS*-only and coupled simulation reach similar accuracy levels, in terms of free surface elevation and inline force on the cylinder. Comparing their respective computational costs is thus relevant.

Consider the $T = 9\,\mathrm{s}$ case with a coupled simulation. The computation runs for 3 days on four 36-cores nodes of the computing

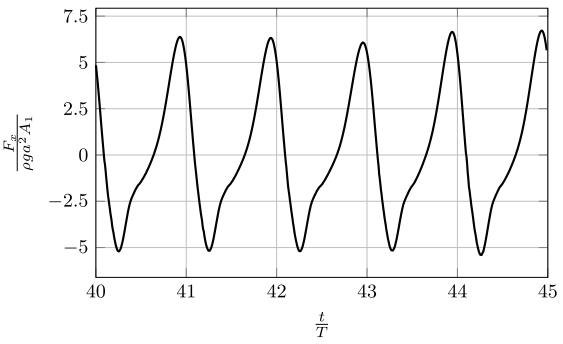

Fig. 22. Normalized horizontal force time signal between $t = 40T$ and $t = 45T$ for $T = 15\,\mathrm{s}$ and $\epsilon = 1/40$.

Table 2
Normalized amplitude of the first three harmonics of the depth-integrated inline force on the cylinder in comparison to experimental results.

ϵ	T		$F_x^{(\omega)}/(\rho g a^2 A_1)$	$F_x^{(2\omega)}/(\rho g a^2 A_1)$	$F_x^{(3\omega)}/(\rho g a^2 A_1)$
1/40	9 s	Experiment	5.75	0.32	0.056
		CS-only	5.55	0.29	0.034
		Coupled	5.84	0.27	0.030
1/40	12 s	Experiment	4.78	0.72	0.014
		Coupled	4.83	0.74	0.078
1/40	15 s	Experiment	4.21	1.29	0.19
		Coupled	4.22	1.36	0.22
1/22	15 s	Experiment	4.21	1.89	0.40
		Coupled	4.57	2.00	0.32

cluster, with 80 processors being attributed to the *CS* instance, while 35 are reserved for *seine3d* 1 and *seine3d* 2. Again, the distribution of computational resources to the different code instances was not studied, and it is very likely not optimal (see e.g., Harris et al., 2022 for a study of the computational time of *seine3d*). 338.22 s were computed, corresponding to $37.58T$. With this setup, simulating one wave period takes 1.75 h. The ratio of computational time to simulated time is therefore:

$$N_{cpl.} = \frac{1.75 \times 36 \times 4}{9} = 28.0 \text{ ch.s}^{-1}$$

A significant variation in computational efficiency was seen between the different cases; for the 15 s period coupled run, the ratio of computational to simulated time was 4.4 ch.s^{-1}, for example.

Alternatively, a *CS*-only simulation with $T = 9\,\mathrm{s}$ and $\epsilon = 1/40$ was run on 27 nodes of 36-cores each of the computing cluster for a 3-days-long computation. $79.3T$ are simulated. Simulating one wave period took 0.76 h. The computational time to simulated time ratio is:

$$N_{\text{CS}} = \frac{0.76 \times 36 \times 27}{9} = 82.1 \text{ ch.s}^{-1}$$

N_{CS} is thus 2.93 higher than the previously computed $N_{cpl.}$ for the total hybrid model. Given that 80 processors are being used for *CS*, this is a reduction by a factor of 3.96 for just the *CS* part, the rest of the CPU time taken up by the *seine3d* instances and the overhead of the coupling code. This result may be seen as conservative, as we also have specified that computational resource allocation is perfectible in the case of coupled simulations. It is also close to the gain obtained using the SWENSE method for a similar problem reported by Li et al. (2021). Notably, no study of the influence of the size of the *CS* numerical domain has been conducted: it might be even smaller, but the same might be said of $L_{overlap}$.

There should be room for improvement, and the computational speed of hybrid computations may well be increased. A detailed scalability analysis of 3D coupled large simulations was nevertheless considered out of the scope of the current work. Nevertheless, it appears that 3D simulations of nonlinear wave diffraction by a vertical cylinder are feasible with the coupling strategy, at a lower computational cost than CFD alone. The limits experienced in 2DV about the accuracy of free surface elevation and velocities explain most of the shortcomings reported in 3D. Therefore emphasis should be put on 2DV highly nonlinear simulations, in the hope that improvements can later be applied to 3D computations.

7. Discussion

The developed coupling strategy has proven to be quite straightforwardly applicable to engineering problems. Reasonable computational costs are achieved even for large computational meshes, made possible by the parallel nature of the hybrid solver. As an example, a 3D wave–structure simulation with $T = 15$ s, $\epsilon = 1/40$, where the *CS* mesh has approximately 650 000 elements while *seine3d* instances meshes respectively have 1181 and 1401 nodes requires 1.22 h to simulate one wave period on 2 computing nodes featuring 27 CPUs. These costs appear to amount to only a fraction – one third, in the only 3D case investigated – of that of *CS*-only similar computations. Thus, this work could enable a more frequent use of CFD tools in the engineering practice. However, additional efforts are needed to gain more insight into the behavior and capabilities of the coupling methodology in its current state. Developments could also be expected to further improve efficiency and expand the range of handled problems. Note that memory requirements are not reported here, but are generally small, a few GB at most, as the problem is primarily limited by CPU time for problems of the scale shown here.

Additional studies related to the use of *seine3d* in its current state, with this hybrid strategy, are needed. The instabilities reported in the coupled *seine3d* instances should be further investigated to understand their origin and to possibly avoid them. Deeper convergence studies could be conducted for coupled simulations, to further validate the method and allow for a finer selection of numerical parameters, as well as more accurate results, for example in terms of higher-order wave forces. In particular, the respective impacts of the time-step ratio and the overlapping length should be better documented. This is no doubt problem dependent, as CFL numbers in NS solvers varies widely depending on the physics. For wave modeling itself, a mesh and time step similar to that of a potential flow model is possible (Ma et al., 2012), whereas for breaking wave impacts on a cylinder a very small time step is required (Li and Fuhrman, 2022). The influence of variations in the characteristics of incident waves, especially their length and period, over the coupled simulations and the choice of the above-mentioned parameters of the coupling, should be studied. Investigations into the distribution of CPU cores over the different coupled code instances and a scalability analysis would be valuable improvements made to the hybrid computations.

In this work, a slip condition is imposed on the surface of the monopile in *CS*, as well as on all the vertical walls. Even though the agreement with experimental results appears to be good, a possible step forward would be to include the effects of turbulent boundary layers in the simulations. As several turbulence models are already available in *CS*, this would only require working on specific boundary conditions for turbulent quantities at the coupled boundaries of *CS* instances. This way, the local shear forces applied on partially submerged structures would be accounted for and an increased accuracy could be reached. Increasing the order of the interpolation schemes used in *CS* to extract the values of the fluid velocity and the free surface elevation needed by a coupled *seine3d* instance is yet another source of improvement. This requires conveniently accessing air fraction and velocity gradient fields in *CS*'s user routines.

Another area of improvement is the generalization of the coupling strategy to unstructured *CS* meshes. Currently, it is only possible to use meshes in which overlapping regions are described with Cartesian grids. This would require the implementation of a new method for computing free surface positions in *CS* as well. This would allow for

easier simulation of wave forces on structures of complex shapes, with body-fitted meshes.

It is also possible to replace *CS* by the two-phase code *neptune_cfd*, which tracks both the air and water velocity in a given cell (as opposed to the single velocity field here), developed by EDF R&D (2022), that shares most of its components with *CS*. It has been recently successfully applied to solve regular wave diffraction problems investigated in the WAS-XL experimental campaign in engineering studies, similarly to what was done with the coupled solver above. It features a porous media approach that allows for a straightforward description of any structure placed in waves, without the need for a complex meshing stage (note that this feature is also planned for a future release of *CS*).

For the moment, some improvements added recently to *seine3d* have not been tested here in the coupled *seine3d* instances. One of these is the use of the Fast Multipole Method that allows for an accelerated solution procedure (Harris et al., 2022). In addition, it might be interesting to evaluate the sensitivity of the coupling procedure to changes made to the time-stepping scheme selected in *seine3d*, as different schemes are already implemented.

As discussed above for the viscous CFD code, alternative potential flow solvers could also be considered using the same coupling strategy developed here. This would allow exploring options to overcome stability issues encountered in several cases here with *seine3d*, and/or possibly reducing the total computational cost of the coupled simulations. In this direction, the recently developed FNPF solvers based on the HPC technique (Robaux and Benoit, 2021) or on a spectral approach in the vertical (Zhang and Benoit, 2021) could be considered, among other options.

8. Conclusions

The definition, implementation, verification and validation through comparisons to analytical solutions and experimental results of a two-way coupling strategy involving a fully nonlinear potential BEM model and a viscous VOF model have been described. This coupling methodology relies on the mutual exchange of fluid velocities between both codes, at the boundaries located at both ends of an overlapping region. It allows the simulation of 3D wave–structure interactions on large spatial and temporal scales, making the most of each code's intrinsic performances and ranges of application. Savings in the computational cost of the simulations were obtained, by a factor of about 3 with reference to a VOF-only simulation on a domain of the same dimensions. If we further consider only the reduction of CPU time from the coupling, *CS* time was reduced by a factor of about 4, giving a sense of the performance advantage possible through an optimized potential model. Multiple couplings may be set through the pairing of different instances of *seine3d* and *CS*, dividing the global domain of interest into several overlapping subdomains. The designed hybrid procedure is intended to introduce the lowest possible number of additional simulation parameters. After choices have been made in each code about the temporal and spatial discretization levels, as well as about the physical assumptions and the solution procedure, theoretically only the length(s) of the overlapping region(s) needs to be set. Stability issues of the hybrid computations with certain values of the CFL number in the models were experienced, indicating that the respective temporal and spatial resolutions affect the applicability of the coupling strategy. The possibility to run massively parallel computations, available in *seine3d* and *CS*, has also been retained.

In the presented 2DV coupled simulations featuring nonlinear regular waves over constant water depth, the wave conditions for a reference experimental campaign focusing on wave interactions with a vertical bottom-mounted circular cylinder are reproduced. In particular, a given wave condition is simulated using each code alone at first, then with the hybrid algorithm to assess the wave generation and absorption techniques in *seine3d* and *CS*. The results are compared with semi-analytical SF wave solutions used for wave generation, in terms of the wave elevation time history, as well as the velocity field underneath the waves. When looking at the vertical structure of the fluid velocity, significant differences with the expected SF profiles were observed, increasing with time, calling for a brief sensitivity analysis of various parameters, aimed at reducing the error levels. Finally, coupled simulations are run for two values of the wave steepness, namely $\epsilon = H/\lambda = 1/40 = 2.5\%$ and $\epsilon = 1/22 \approx 4.5\%$. It is believed that the rules used to set spatial and temporal discretization levels as well as various other numerical parameters in 2DV still hold for more complex 3D cases.

Finally, the hybrid 3D simulations are validated through comparison with experiments (WAS-XL campaign, Dadmarzi et al., 2019) about regular wave diffraction by a vertical cylinder. Three wave conditions with a moderate wave steepness of $\epsilon = 1/40$ are tested, while the monopile radius and the water depth are kept constant. A satisfactory agreement between simulated and experimental results is found in terms of the wave elevation close to the vertical cylinder and the depth-integrated inline force on the cylinder. Computed higher-order force components match the experimental ones reasonably well up to third-order. For one wave condition, a *CS*-only simulation is realized that reaches accuracy levels similar to those of its hybrid counterpart, but at a greater computational cost. A case with $\epsilon = 1/22$ shows that coupled simulations of steep regular waves are feasible within the coupled framework, with, however, higher error levels with respect to experimental measurements.

In future work, the simulation of irregular and/or multidirectional waves, possibly traveling over variable bathymetry could be conducted following the coupling strategy. Phase-focused wave impacts with possible wave breaking could also be investigated, similar to the one-way coupling used in Batlle Martin et al. (2023). Making the most of the versatile nature of the hybrid solver, one might also use more complex overlapping regions geometry. Indeed, coupling regions having the form of rectangular or circular rings could quite easily be defined, enabling 3D simulations of waves interacting with multiple structures. Last but not least, the potential-CFD coupling procedure could be used alongside with a fluid/structure coupling approach, so that interactions of waves with moving structures could be handled. This is of particular interest for the study of floating offshore wind turbines, which is a promising solution for harvesting wind energy in greater water depths.

CRediT authorship contribution statement

Paul Landesman: Writing – original draft, Visualization, Validation, Software, Methodology. **Jeffrey C. Harris:** Writing – review & editing, Supervision, Software, Methodology. **Christophe Peyrard:** Writing – review & editing, Supervision, Project administration. **Michel Benoit:** Writing – review & editing, Supervision, Methodology.

Declaration of competing interest

The authors declare that they have no known competing financial interests or personal relationships that could have appeared to influence the work reported in this paper.

Data availability

Data will be made available on request.

Acknowledgments

The work of Paul Landesman was funded by the Association Nationale de la Recherche et de la Technologie (ANRT), CIFRE agreement no. 2018/0235. The authors would like to thank Yvan Fournier (EDF R&D, MFEE, Chatou, France) and Prof. Stephan Grilli (Univ. Rhode Island, USA) for their helpful discussions.

References

Archambeau, F., Méchitoua, N., Sakiz, M., 2004. Code Saturne: A Finite Volume Code for the computation of turbulent incompressible flows - Industrial Applications. Int. J. Finite Vol. 1 (1), 1–62.

Bai, W., Eatock Taylor, R., 2007. Numerical simulation of fully nonlinear regular and focused wave diffraction around a vertical cylinder using domain decomposition. Appl. Ocean Res. 29 (1–2), 55–71. http://dx.doi.org/10.1016/j.apor.2007.05.005.

Batlle Martin, M., Harris, J.C., Filipot, J.F., Hulin, F., Tassin, A., Renaud, P., 2023. Deep water focused breaking wave loads on a fixed cylinder. Coast. Eng. 186, 104397. http://dx.doi.org/10.1016/j.coastaleng.2023.104397.

Batlle Martin, M., Harris, J.C., Renaud, P., Hulin, F., Filipot, J.F., 2022. Numerical investigation of slamming loads on floating offshore wind turbines. In: The 32nd International Ocean and Polar Engineering Conference. OnePetro, pp. 212–217.

Campana, E., Di Mascio, A., Esposito, P., Lalli, F., 1995. Viscous-inviscid coupling in free surface ship flows. Internat. J. Numer. Methods Fluids 21 (9), 699–722. http://dx.doi.org/10.1002/fld.1650210902.

Chen, H.C., Lee, S.K., 1999. RANS/Laplace calculations of nonlinear waves induced by surface-piercing bodies. J. Eng. Mech. 125 (11), 1231–1242. http://dx.doi.org/10.1061/(ASCE)0733-9399(1999)125:11(1231).

Chorin, A.J., 1968. Numerical solution of the Navier-Stokes equations. Math. Comput. 22 (104), 745–762. http://dx.doi.org/10.2307/2004575.

Code Saturne development team, 2019. Code_Saturne 6.0.0 theory guide. URL: https://www.code-saturne.org/documentation/6.0/theory.pdf. (Accessed 02 February 2022).

Colicchio, G., Greco, M., Faltinsen, O., 2006. A BEM-level set domain-decomposition strategy for non-linear and fragmented interfacial flows. Internat. J. Numer. Methods Engrg. 67 (10), 1385–1419. http://dx.doi.org/10.1002/nme.1680.

Dadmarzi, F.H., Thys, M., Bachynski, E.E., 2019. Validation of hydrodynamic loads on a large-diameter monopile in regular waves. In: Proceedings of the ASME 2019 38th International Conference on Ocean, Offshore and Arctic Engineering OMAE2019. In: International Conference on Offshore Mechanics and Arctic Engineering, vol. 7A: Ocean Engineering, ASME, pp. 1–8. http://dx.doi.org/10.1115/OMAE2019-95929.

Darwish, M., Moukalled, F., 2006. Convective schemes for capturing interfaces of free-surface flows on unstructured grids. Numer. Heat Transfer B 49 (1), 19–42. http://dx.doi.org/10.1080/10407790500272137.

Dean, R.G., 1965. Stream function representation of nonlinear ocean waves. J. Geophys. Res. 70, 4561–5472. http://dx.doi.org/10.1029/JZ070i018p04561.

Di Paolo, B., Lara, J.L., Barajas, G., Losada, Í.J., 2021. Wave and structure interaction using multi-domain couplings for Navier-Stokes solvers in OpenFOAM. Part I: Implementation and validation. Coast. Eng. 164, 103799. http://dx.doi.org/10.1016/j.coastaleng.2020.103799.

Dias, F., Bridges, T., 2006. The numerical computation of freely propagating time-dependent irrotational water waves. Fluid Dyn. Res. 38, 803–830. http://dx.doi.org/10.1016/j.fluiddyn.2005.08.007.

Ducrozet, G., Engsig-Karup, A.P., Bingham, H.B., Ferrant, P., 2014. A non-linear wave decomposition model for efficient wave–structure interaction. Part A: Formulation, validations and analysis. J. Comput. Phys. 257, 863–883. http://dx.doi.org/10.1016/j.jcp.2013.09.017.

EDF R&D, 2022. Neptune solver. URL: https://www.code-saturne.org/cms/web/NEPTUNECFD. (Accessed 25 January 2022).

Fenton, J.D., 1999. Numerical methods for nonlinear waves. In: Liu, P.L.F. (Ed.), Advances in Coastal and Ocean Engineering. World Scientific Pub. Co. Inc., pp. 241–324.

Ferrant, P., 1998. Fully nonlinear interactions of long-crested wave packets with a three-dimensional body. In: Proc. 22nd ONR Symposium on Naval Hydrodynamics. Washington DC., USA, pp. 403–416.

Fochesato, C., Grilli, S.T., Guyenne, P., 2005. Note on non-orthogonality of local curvilinear co-ordinates in a three-dimensional boundary element method. Internat. J. Numer. Methods Fluids 48, 305–324. http://dx.doi.org/10.1002/fld.838.

Fournier, Y., 2020. Massively parallel location and exchange tools for unstructured meshes. Int. J. Comput. Fluid Dyn. 34 (7–8), 549–568. http://dx.doi.org/10.1080/10618562.2020.1810676.

Gentaz, L., Luquet, R., Alessandrini, B., Ferrant, P., 2004. Numerical simulation of the 3D viscous flow around a vertical cylinder in non-linear waves using an explicit incident wave model. In: International Conference on Offshore Mechanics and Arctic Engineering, Vol. 37432. pp. 157–163.

Goda, Y., Suzuki, T., 1976. Estimation of incident and reflected waves in random wave experiments. In: Proc. Int. Conf. on Coastal Engineering, Vol. 1, No. 15. ICCE1976, pp. 828–845. http://dx.doi.org/10.9753/icce.v15.47.

Gottlieb, S., 2005. On high order strong stability preserving Runge–Kutta and multi step time discretizations. J. Sci. Comput. 25, 105–128. http://dx.doi.org/10.1007/BF02728985.

Greco, M., 2002. Water shipping on a vessel in head waves. In: 24th Symposium on Naval Hydrodynamics Fukuoka. Japan, 2002, pp. 40–52.

Greco, M., Faltinsen, O., Landrini, M., 2002. Numerical simulation of heavy water shipping. In: Proc. 17th Workshop on Water Waves and Floating Bodies. Cambridge UK, pp. 14–16.

Grilli, S.T., Guyenne, P., Dias, F., 2001. A fully nonlinear model for three-dimensional overturning waves over arbitrary bottom. Internat. J. Numer. Methods Fluids 35, 829–867. http://dx.doi.org/10.1002/1097-0363(20010415)35:7%3C829::AID-FLD115%3E3.0.CO;2-2.

Grilli, S.T., Horrillo, J., 1997. Generation and absoption of fully nonlinear periodic waves. J. Eng. Mech. 123, 1060–1069. http://dx.doi.org/10.1061/(ASCE)0733-9399(1997)123:10(1060).

Guignard, S., Grilli, S.T., Marcer, R., Rey, V., 1999. Computation of shoaling and breaking waves In Nearshore Areas by the coupling of BEM and VOF methods. In: International Ocean and Polar Engineering Conference. ISOPE99, Brest, France, pp. 304–309.

Guo, L., Sun, D., Hao, W., 2012. A new numerical wave flume combining the 0–1 type BEM and the VOF method. J. Hydrodyn. Ser. B 24 (4), 506–517. http://dx.doi.org/10.1016/S1001-6058(11)60272-2.

Hamilton, J.A., Yeung, R.W., 2011. Viscous and inviscid matching of three-dimensional free-surface flows utilizing shell functions. J. Engrg. Math. 70 (1–3), 43–66. http://dx.doi.org/10.1007/s10665-010-9438-0.

Hanssen, F.C.W., 2019. Non-Linear Wave-Body Interaction in Severe Waves (Ph.D. thesis). Norwegian University of Science and Technology (NTNU), Norway.

Harris, J.C., Dombre, E., Benoit, M., Grilli, S.T., Kuznetsov, K.I., 2022. Nonlinear time-domain wave-structure interaction: a parallel fast integral equation approach. Internat. J. Numer. Methods Fluids 94 (2), 188–222. http://dx.doi.org/10.1002/fld.5051.

Harris, J.C., Grilli, S.T., 2012. A perturbation approach to large eddy simulation of wave-induced bottom boundary layer flows. Internat. J. Numer. Methods Fluids 68 (12), 1574–1604. http://dx.doi.org/10.1002/fld.2553.

Hayami, K., Matsumoto, H., 1994. Improvement of quadrature for nearly singular integrals in 3D-BEM. WIT Trans. Model. Simul. 7.

Hildebrandt, A., Sriram, V., 2014. Pressure distribution and vortex shedding around a cylinder due to a steep wave at the onset of breaking from physical and numerical modeling. In: The Twenty-Fourth International Ocean and Polar Engineering Conference. Busean, Korea, pp. 405–410.

Hirt, C., Nichols, B., 1981. Volume of fluid (VOF) method for the dynamics of free boundaries. J. Comput. Phys. 39 (1), 201–225. http://dx.doi.org/10.1016/0021-9991(81)90145-5.

Iafrati, A., Campana, E., 2003. A domain decomposition approach to compute wave breaking (wave-breaking flows). Internat. J. Numer. Methods Fluids 41 (4), 419–445. http://dx.doi.org/10.1002/fld.448.

Kemper, J., Windt, C., Graf, K., Ringwood, J., 2019. Development towards a nested hydrodynamic model for the numerical analysis of ocean wave energy systems. In: European Tidal and Wave Energy Conference Proceedings, No. 1414. EWTEC, Napoli, Italy, p. 10.

Kim, S.H., Yamashiro, M., Yoshida, A., 2010. A simple two-way coupling method of BEM and VOF model for random wave calculations. Coast. Eng. 57 (11–12), 1018–1028. http://dx.doi.org/10.1016/j.coastaleng.2010.06.006.

Lachaume, C., Biausser, B., Fraunié, P., Grilli, S.T., Guignard, S., 2003. Modeling of breaking and post-breaking waves on slopes by coupling of BEM and VOF methods. In: The Thirteenth International Offshore and Polar Engineering Conference. pp. 353–359.

Landesman, P., 2022. Simulation of Wave-Structure Interaction by a Two-Way Coupling Between a Fully Nonlinear Potential Flow Model and a Navier-Stokes Solver (Ph.D. thesis). Ecole des Ponts ParisTech, Marne-la-Vallée, France.

Larsen, B.E., Fuhrman, D.R., Roenby, J., 2019. Performance of interfoam on the simulation of progressive waves. Coast. Eng. J. 61 (3), 380–400. http://dx.doi.org/10.1080/21664250.2019.1609713.

Li, Z., Bouscasse, B., Ducrozet, G., Gentaz, L., Le Touzé, D., Ferrant, P., 2021. Spectral Wave Explicit Navier-Stokes Equations for wave-structure interactions using two-phase Computational Fluid Dynamics solvers. Ocean Eng. 221, 108513. http://dx.doi.org/10.1016/j.oceaneng.2020.108513.

Li, Y., Fuhrman, D.R., 2022. On the turbulence modelling of waves breaking on a vertical pile. J. Fluid Mech. 953, A3. http://dx.doi.org/10.1017/jfm.2022.941.

Longuet-Higgins, M.S., Cokelet, E., 1976. The deformation of steep surface waves on water, I. A numerical method of computation. Proc. R. Soc. Lond. Ser. A Math. Phys. Eng. Sci. 350, 1–26. http://dx.doi.org/10.1098/rspa.1976.0092.

Lu, X., Chandar, D.D.J., Chen, Y., Lou, J., 2017. An overlapping domain decomposition based near-far field coupling method for wave structure interaction simulations. Coast. Eng. 126, 37–50. http://dx.doi.org/10.1016/j.coastaleng.2017.04.009.

Ma, G., Shi, F., Kirby, J.T., 2012. Shock-capturing non-hydrostatic model for fully dispersive surface wave processes. Ocean Model. 43, 22–35. http://dx.doi.org/10.1016/j.ocemod.2011.12.002.

Mintgen, F., Manhart, M., 2018. A bi-directional coupling of 2D shallow water and 3D Reynolds-averaged Navier–Stokes models. J. Hydraul. Res. 56 (6), 771–785. http://dx.doi.org/10.1080/00221686.2017.1419989.

Monroy, C., Ducrozet, G., Bonnefoy, F., Babarit, A., Gentaz, L., Ferrant, P., 2011. RANS simulations of a CALM buoy in regular and irregular seas using the SWENSE method. In: The Twentieth International Offshore and Polar Engineering Conference. Beijing, China, pp. 264–271.

Morison, J., Johnson, J., Schaaf, S., 1950. The force exerted by surface waves on piles. J. Pet. Technol. 2 (05), 149–154. http://dx.doi.org/10.2118/950149-G.

Muzaferija, S., 1999. A two-fluid Navier-Stokes solver to simulate water entry. In: Proceedings of 22nd Symposium on Naval Architecture, 1999. National Academy Press, pp. 638–651.

O'Reilly, C.M., Grilli, S.T., Janßen, C.F., Dahl, J.M., Harris, J.C., 2022. Hybrid Lattice-Boltzmann-potential flow simulations of turbulent flow around submerged structures. J. Mar. Sci. Eng. 10 (11), 1651. http://dx.doi.org/10.3390/jmse10111651.

Paulsen, B., 2013. Efficient Computations of Wave Loads on Offshore Structures (Ph.D. thesis). Technical University of Denmark, Denmark.

Paulsen, B.T., Bredmose, H., Bingham, H.B., Jacobsen, N.G., 2014. Forcing of a bottom-mounted circular cylinder by steep regular water waves and finite depth. J. Fluid Mech. 755, 1–34. http://dx.doi.org/10.1017/jfm.2014.386.

Pringle, W.J., Yoneyama, N., Mori, N., 2016. Two-way coupled long wave-RANS model: Solitary wave transformation and breaking on a plane beach. Coast. Eng. 114, 99–118. http://dx.doi.org/10.1016/j.coastaleng.2016.04.011.

Renaud, P., Martin, M.B., Hulin, F., Harris, J.C., Filipot, J.F., Scolan, Y.M., 2023. Semi-analytical load models describing the progressive immersion of a fixed vertical cylinder in a breaking wave. Ocean Eng. 276, 114116. http://dx.doi.org/10.1016/j.oceaneng.2023.114116.

Robaux, F., 2020. Numerical Simulation of Wave-Body Interaction: Development of a Fully Nonlinear Potential Flow Solver and Assessment of Two Local Coupling Strategies with a CFD Solver (Ph.D. thesis). Aix Marseille University, Marseille, France.

Robaux, F., Benoit, M., 2021. Development and validation of a numerical wave tank based on the harmonic polynomial cell and immersed boundary methods to model nonlinear wave-structure interaction. J. Comput. Phys. 446, 110560. http://dx.doi.org/10.1016/j.jcp.2021.110560.

Robaux, F., Benoit, M., 2022. Assessment of one-way coupling methods from a potential to a viscous flow solver based on domain-and functional-decomposition for fixed submerged bodies in nonlinear waves. Eur. J. Mech. B Fluids 95, 315–334. http://dx.doi.org/10.1016/j.euromechflu.2022.05.011.

Saincher, S., Sriram, V., 2022. A three dimensional hybrid fully nonlinear potential flow and Navier Stokes model for wave structure interactions. Ocean Eng. 266, 112770. http://dx.doi.org/10.1016/j.oceaneng.2022.112770.

Siddiqui, M.A., Greco, M., Colicchio, G., Faltinsen, O.M., 2018. Validation of damaged ship hydrodynamics by a domain decomposition approach using the harmonic polynomial cell method and openfoam. In: Proceedings of 33rd International Workshop on Water Waves and Floating Bodies. Guidel-Plage, France, p. 4.

Sitanggang, K., Lynett, P., 2010. Multi-scale simulation with a hybrid Boussinesq-RANS hydrodynamic model. Internat. J. Numer. Methods Fluids 62 (9), 1013–1046. http://dx.doi.org/10.1002/fld.2056.

Sriram, V., Ma, Q., Schlurmann, T., 2014. A hybrid method for modelling two dimensional non-breaking and breaking waves. J. Comput. Phys. 272, 429–454. http://dx.doi.org/10.1016/j.jcp.2014.04.030.

Sueyoshi, M., Kihara, H., Kashiwagi, M., 2007. A hybrid technique using particle and boundary-element methods for wave-body interaction problems. In: Proceedings of the 9th International Conference on Numerical Ship Hydrodynamics, Vol. 1. Ann Harbor, Michignan, USA, pp. 241–252.

United Nations, 2015. The Paris agreement. URL: https://unfccc.int/process-and-meetings/the-paris-agreement/the-paris-agreement. (Accessed 24 January 2022).

Veic, D., Sulisz, W., 2018. Impact pressure distribution on a monopile structure excited by irregular breaking wave. Pol. Marit. Res. 25 (s1), 29–35. http://dx.doi.org/10.2478/pomr-2018-0019.

Verbrugghe, T., Domínguez, J.M., Crespo, A.J., Altomare, C., Stratigaki, V., Troch, P., Kortenhaus, A., 2018. Coupling methodology for smoothed particle hydrodynamics modelling of non-linear wave-structure interactions. Coast. Eng. 138, 184–198. http://dx.doi.org/10.1016/j.coastaleng.2018.04.021.

Verbrugghe, T., Stratigaki, V., Altomare, C., Domínguez, J., Troch, P., Kortenhaus, A., 2019. Implementation of open boundaries within a two-way coupled SPH model to simulate nonlinear wave–structure interactions. Energies 12 (4), 697. http://dx.doi.org/10.3390/en12040697.

Versteeg, H.K., Malalasekera, W., 2007. An Introduction to Computational Fluid Dynamics: The Finite Volume Method. Pearson Education.

Wind Europe, 2021. Wind energy in Europe 2020 Statistics and the outlook for 2021–2025. URL: https://windeurope.org/intelligence-platform/product/wind-energy-in-europe-in-2020-trends-and-statistics/#downloads. (Accessed 24 January 2022).

Yan, S., Ma, Q., 2017. A Hybrid Approach Coupling MLPG-R With QALE-FEM for Modelling Fully Nonlinear Water Waves. In: International Ocean and Polar Engineering Conference. ISOPE2017, San Francisco, California, USA, pp. 654–661.

Zhang, J., Benoit, M., 2021. Wave–bottom interaction and extreme wave statistics due to shoaling and de-shoaling of irregular long-crested wave trains over steep seabed changes. J. Fluid Mech. 912, A28. http://dx.doi.org/10.1017/jfm.2020.1125.

Zhang, D., Jiang, C., Liang, D., Chen, Z., Yang, Y., Shi, Y., 2014. A refined volume-of-fluid algorithm for capturing sharp fluid interfaces on arbitrary meshes. J. Comput. Phys. 274, 709–736. http://dx.doi.org/10.1016/j.jcp.2014.06.043.

Zhang, Y., Peszynska, M., Yim, S., 2013. Coupling of viscous and potential flow models with free surface for near and far field wave propagation. Int. J. Numer. Anal. Model. 4 (3), 256–282.